REPORT DOCUMENTATION PAGE

Form Approved
OMB No. 0704-0188

Public reporting burden for this collection of information is estimated to average 1 hour per response, including the time for reviewing instructions, searching existing data sources, gathering and maintaining the data needed, and completing and reviewing the collection of information. Send comments regarding this burden estimate or any other aspect of this collection of information, including suggestions for reducing this burden, to Department of Defense, Washington Headquarters Services, Directorate for Information Operations and Reports (0704-0188), 1215 Jefferson Davis Highway, Suite 1204, Arlington, VA 22202-4302. Respondents should be aware that notwithstanding any other provision of law, no person shall be subject to any penalty for failing to comply with a collection of information if it does not display a currently valid OMB control number.
PLEASE DO NOT RETURN YOUR FORM TO THE ABOVE ADDRESS.

1. REPORT DATE (DD-MM-YYYY) 05-02-2010	2. REPORT TYPE FINAL	3. DATES COVERED (From – To) November 08, 2007–November 07, 2009

4. TITLE AND SUBTITLE	5a. CONTRACT NUMBER FA9550-08-C-0035
A Simulation Environment for Aerodynamic Analysis and Design of Flapping Wing Micro Air Vehicles	5b. GRANT NUMBER
Final Report for STTR Phase 2 Project	5c. PROGRAM ELEMENT NUMBER

6. AUTHOR(S)	5d. PROJECT NUMBER
Dr. Siddharth Thakur (352) 271-8841 Dr. Jeffrey Wright Dr. Wei Shyy Dr. Luis Bernal	5e. TASK NUMBER
	5f. WORK UNIT NUMBER

7. PERFORMING ORGANIZATION NAME(S) AND ADDRESS(ES) Streamline Numerics, Inc. 3221 NW 13th Street, Suite A Gainesville, FL 32609	8. PERFORMING ORGANIZATION REPORT NUMBER SNI-CR-2010-1

9. SPONSORING/MONITORING AGENCY NAME(S) AND ADDRESS(ES) Program Manager: Douglas Smith AFOSR/NA, 875 N. Randolph Street, Room 3112 Arlington, VA 22203	10. SPONSORING/MONITOR'S ACRONYM(S)
	11. SPONSORING/MONITORING REPORT NUMBER AFRL-AFSOR-VA-TR-2016-0647

12. DISTRIBUTION/AVAILABILITY STATEMENT
Approved for public release; distribution unlimited.

13. SUPPLEMENTARY NOTES

14. ABSTRACT
The overall goal of the work conducted in this project was to develop a combined simulation and experimental capability to further the understanding of unsteady wing aerodynamics of flapping micro air vehicles (MAVs) and to assist in design of such vehicles. The primary objective of the overall effort was to develop and validate a simulation environment with high-fidelity modeling of flapping-wing MAV flight physics. The next objective was to study the fluid physics associated with low Reynolds number flapping wings to facilitate the design of effective high-bandwidth control of wing beat kinematics for MAVs. Another objective was to build a fundamental knowledge base for the physics of flapping wing Micro Air Vehicles (MAVs). This Phase 2 work had two major components: (a) Simulation environment based on an advanced Computational Fluid Dynamics (CFD) solver called Loci-STREAM, and, (b) Experimental effort to validate the simulations and to guide model development.

15. SUBJECT TERMS
MAV design tool, Flapping wing, Loci-STREAM code.

16. SECURITY CLASSIFICATION OF:			17. LIMITATION OF ABSTRACT	18. NUMBER OF PAGES	19a. NAME OF RESPONSIBLE PERSON Dr. Siddharth Thakur
a. REPORT U	b. ABSTRACT U	c. THIS PAGE U	UU	178	19b. TELEPHONE NUMBER (Include area code) (352) 271-8841

STTR PHASE 2 PROJECT FINAL REPORT

Contract Number FA9550-08-C-0035

A Simulation Environment for Aerodynamic Analysis and Design of Flapping Wing Micro Air Vehicles

Siddharth Thakur & Jeffrey Wright
Streamline Numerics
Gainesville, FL 32609

Wei Shyy & Luis Bernal
University of Michigan
Ann Arbor, MI

January, 2010

CONTENTS

1. PROJECT SUMMARY

The overall goal of the work conducted in this project was to develop a combined simulation and experimental capability to further the understanding of unsteady wing aerodynamics of flapping micro air vehicles (MAVs) and to assist in design of such vehicles. The primary objective of the overall effort was to develop and validate a simulation environment with high-fidelity modeling of flapping-wing MAV flight physics. The next objective was to study the fluid physics associated with low Reynolds number flapping wings to facilitate the design of effective high-bandwidth control of wing beat kinematics for MAVs. Another objective was to build a fundamental knowledge base for the physics of flapping wing Micro Air Vehicles (MAVs). The Phase 2 work had two major components:

- Simulation environment based on an advanced Computational Fluid Dynamics (CFD) solver called Loci-STREAM, and
- Experimental effort to validate the simulations and to guide model development.

Loci-STREAM served as the simulation tool for investigating flapping wing aerodynamics. Several pitching and plunging airfoil cases were investigated during this project which demonstrated the need for accurate and efficient CFD capability to resolve the unsteady flow fields associated with flapping wings. The simulations demonstrated that a variation of the Reynolds number (wing sizing, flapping frequency, etc) leads to changes in the leading edge vortex (LEV) and spanwise flow structures, which impact the aerodynamic force generation. While in classical stationary wing theory the tip vortices (TiVs) are seen as wasted energy, in flapping flight, they can interact with the LEV to enhance lift without increasing the power requirements. Surrogate modeling techniques can assess the aerodynamic outcomes between two- and three-dimensional wings. The combined effect of the TiVs, the LEV, and jet can improve the aerodynamics of a flapping wing. Efforts are continuing in broadening Loci-STREAM's capability to address aeroelasticity. In particular, chordwise flexibility in the forward flight can substantially adjust the projected area normal to the flight trajectory via shape deformation, hence redistributing thrust and lift. Spanwise flexibility in the forward flight creates shape deformation from the wing root to the wing tip resulting in varied phase shift and effective angle of attack distribution along the wing span. Numerous open issues in flapping wing aerodynamics along these lines exist. Additionally, numerous issues exist with regards to the computational techniques needed to model such flow fields. Several such issues were addressed during this project such as advanced grid movement techniques, fluid-structure interaction capability, etc. While the simulation tool is still being developed and refined, significant advancement is expected once the tool reaches the intended potential in the near future.

On the experimental side, investigations were conducted on model geometries to validate the CFD capability and to assist in model development. Pitching and plunging airfoil at Reynolds number, Re=10,000, and pure sinusoidal effective angle of attack motion has been investigated. The experiments were conducted at the University of Michigan low-turbulence water channel facility using 2D phase-averaged particle image velocimetry (PIV). The effect of non-dimensional parameters governing pitching and plunging motion such as Strouhal number (St), reduced frequency (k), and the plunge amplitude (h_0) was investigated for the same effective angle of attack kinematics. The formation of a leading edge vortex (LEV) and a trailing edge vortex (TEV) was observed for all the cases studied. The formation phase of the LEV was found to be dependent on k; the LEV formation is delayed for higher k value. It was found that for cases with the same k the velocity profiles normal to the airfoil surface closely follow each other in all cases independent of pitch rate and pivot point effect. Analysis on the locations of the LEV core based on the Q-criterion and local streamline patterns helped identify the trajectory of the LEV core with respect to the airfoil. Additionally, a trend in the LEV circulation was observed.

2. DEVELOPMENT OF COMPUTATIONAL FRAMEWORK

2.1 A High-Fidelity Parallel Simulation Environment for Flapping Wing MAVs: Loci-STREAM

One of the main objectives of this project was to demonstrate an efficient, high-fidelity simulation tool which can be used to enhance the understanding of MAV fluid physics and to assist in the design of such vehicles. A high-fidelity simulation capability requires the use of a full unsteady, viscous, Navier-Stokes based CFD methodology. Over the past decade, such a methodology has been developed by Streamline Numerics resulting in a code called Loci-STREAM for large scale parallel CFD applications (with funding from NASA). The Loci-STREAM code which has been developed within a novel programming framework called Loci (developed at the Mississippi State University). Loci-STREAM has several key features which make it a very attractive framework as an MAV flow simulation and design tool:

- The basic algorithm is an unsteady, pressure-based finite volume method, which is ideal for low Mach number flows including truly incompressible flows, which are typical of MAVs.

- The algorithm has been developed for generalized unstructured grids (employing arbitrarily shaped polyhedra) which allows great flexibility and economy in grid generation for complex geometries such as MAVs (involving wing-body junctions).

- The Loci programming environment facilitates efficient large-scale parallel computing which will allow the simulation of grid-independent, three-dimensional unsteady flows around MAVs with fast turnaround times.

The work involved developing the foundation for the advanced high-fidelity simulation environment in the Loci-STREAM CFD software package, involving advanced mesh movement and robust unsteady modeling capabilities that are essential for modeling MAV flight physics. The basic grid movement algorithm was incorporated into Loci-STREAM. Following that, test cases for the translation and rotation of both thin membranes and airfoils were used to demonstrate that the grid movement algorithm is capable of allowing large geometric deflections (on the order of the body size) even in the presence of highly-refined viscous grids, while still maintaining sufficient grid quality.

2.2 Loci-STREAM: Algorithm for Moving Boundary Problems

Loci-STREAM is a parallelized unstructured curvilinear pressure-based finite-volume code with moving grid capabilities. In the algorithm employed in Loci-STREAM, the momentum and pressure equations are segregated and the solution is advanced using an implicit geometrically conservative time integration method. The convection terms are treated using the second order upwind scheme while pressure and viscous terms are treated using second order schemes. The geometric conservation law, a necessary consideration in domains with moving boundaries, is satisfied.A detailed description of the method implemented in two-dimensions is given elsewhere (Wright and Smith 2001, Smith and Wright 2004). Here we present the main governing equations very briefly; the governing equations for the numerical simulation are the RANS equations coupled with Menter's SST model (Menter 1994), and the continuity equation for incompressible flow,

$$\frac{\partial}{\partial x_i}(u_i) = 0$$

$$\frac{\partial}{\partial t}(u_i) + \frac{\partial}{\partial x_j}(u_j u_i) = -\frac{1}{\rho}\frac{\partial p}{\partial x_i} + \frac{\partial}{\partial x_j}\left\{(\nu + \nu_t)\frac{\partial u_i}{\partial x_j}\right\}$$

5

$$\nu_t = \frac{a_1 k}{\max(a_1 \omega, S\, F_2)}$$

$$\tau_{ij} = \rho \nu_t \left(\frac{\partial u_i}{\partial x_j} + \frac{\partial u_j}{\partial x_i} \right) - \frac{2}{3} \rho k \delta_{ij}$$

$$\frac{\partial k}{\partial t} + \frac{\partial}{\partial x_j}\left(u_j k \right) = \hat{P}_k - \beta^* \omega k + \frac{\partial}{\partial x_j}\left\{ (\nu + \sigma_k \nu_t) \frac{\partial k}{\partial x_j} \right\} \quad\quad (2.1)$$

$$\frac{\partial \omega}{\partial t} + \frac{\partial}{\partial x_j}\left(u_j \omega \right) = -\frac{\gamma}{\nu_t} \frac{\tau_{ij}}{\rho} \frac{\partial u_i}{\partial x_j} - \beta \omega^2 + \frac{\partial}{\partial x_j}\left\{ (\nu + \sigma_\omega \nu_t) \frac{\partial \omega}{\partial x_j} \right\}$$

where $a_1, \beta, \beta^*, \gamma, \sigma_k, \sigma_\omega, F_2$ are defined as in Menter's SST formulation u_i is the velocity component in the ith direction, x_i is the ith component of the position vector, t is time, ρ is density, p is pressure, ν is the kinematic viscosity, ν_t is the eddy viscosity, $S = \sqrt{2S_{ij}S_{ij}}$ is the invariant measure of the strain rate. Compared to Menter's original SST turbulence model a limiter has been built in (Menter 2003) to the production term, $\hat{P}_k$, in the turbulence kinetic energy (TKE) equation, Eq. (1), as

$$P_k = \mu_t \frac{\partial u_i}{\partial x_j}\left(\frac{\partial u_i}{\partial x_j} + \frac{\partial u_j}{\partial x_i} \right),$$

$$\hat{P}_k = \min(P_k, 10 \cdot \beta^* \rho k \omega),$$

where P_k is the production term in the original SST formulation, to prevent the build-up of turbulence in stagnation regions. Another change is the use of invariant measure of the strain-rate tensor in the formulation for the eddy viscosity instead of the vorticity magnitude, $\Omega = \sqrt{2\Omega_{ij}\Omega_{ij}}$. The strain-rate invariant is considered to be a better measure for the fluid deformation, since the Boussinesq approximation is also based on the strain-rate. The two differences between the original and the modified SST formulation are summarized in Table 2.2-1.

Table 2.2-1. Original and modified SST turbulence model

	Original SST	Modified SST
Production term of TKE equation	$P_k = \mu_t \dfrac{\partial u_i}{\partial x_j}\left(\dfrac{\partial u_i}{\partial x_j} + \dfrac{\partial u_j}{\partial x_i} \right)$	$\hat{P}_k = \min(P_k, 10 \cdot \beta^* \rho k \omega)$
Eddy viscosity	$\nu_t = \dfrac{a_1 k}{\max(a_1 \omega, \Omega\, F_2)}$	$\nu_t = \dfrac{a_1 k}{\max(a_1 \omega, S\, F_2)}$

Loci-STREAM has been demonstrated to exhibit near-linear scalability for general incompressible/compressible, turbulent flows using unstructured meshes. Loci-STREAM operates with near-linear scalability for both shared-memory and distributed-memory computer architectures, as shown in Figure 2.2-1.
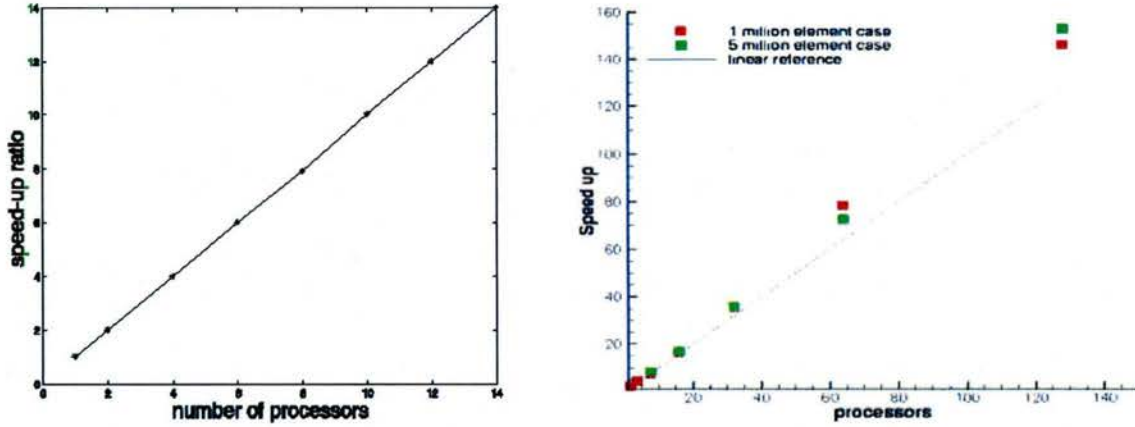
Figure 2.2-1. Speed-up ratio for a typical problem using Loci-STREAM on: (a) shared memory architecture, and (b) distributed memory architecture.

The equation governing the static equilibrium of a homogeneous linear elastic solid in the absence of body forces expressed in terms of displacements is the Navier-Cauchy equation

$$(1-\frac{1}{2\upsilon})\nabla(\nabla \cdot u) + \nabla^2 u = \boldsymbol{0} \tag{2.2}$$

where $\boldsymbol{u}$ is the small displacement vector measured with respect to an undeformed reference configuration and ν is Poisson's ratio. Solutions to Eq. (2.2), obtained under appropriate boundary conditions, are used to update the nodal coordinates according to

$$\boldsymbol{x}^{n+1} = \boldsymbol{x}^n + \boldsymbol{u} \tag{2.3}$$

where $\boldsymbol{x}^{n+1}$ and $\boldsymbol{x}^n$ are the nodal coordinates at the current and previous time levels, respectively. For portions of the computational domain boundary subject to motion, Dirichlet boundary conditions are imposed according to

$$\boldsymbol{u} = g(t) \; on \; \Gamma_f \tag{2.4}$$

where $g(t)$ prescribes the displacement of boundary nodes and Γ_f is the moving portion of the domain boundary. Other boundary conditions such as stress-free or symmetry conditions may be imposed on other portions of the domain boundary to accommodate specific kinematic and geometric situations.

Integrating Eq. (2.2) over a the same control volume used to discretize the momentum equation gives the Navier-Cauchy equation in weak form as

$$\frac{1}{(1-2\upsilon)} \oint_{\Omega d}\nabla(\nabla \cdot u)d\Omega + \oint_{\Omega d}(\nabla \cdot \nabla u)d\Omega = \boldsymbol{0} \tag{2.5}$$

where Ω_d is the control volume.

Following Stein and Tezduyar (2002), the stiffness of an individual control volume in the mesh is modified based on its volume at the current time step. In a face/edge-based finite volume method such as the one used

7

here, control volumes are modified on an edge basis according to

$$\left(\frac{1}{\Omega_e}\right) \Rightarrow \left(\frac{1}{\Omega_e}\right)\left(\frac{\Omega_e}{\Omega_{ref}}\right)^{-\chi}$$ (2.6)

where χ is the stiffening parameter, Ω_e is the edge contribution to the dual control volume and Ω_{ref} is an arbitrary reference volume introduced to maintain dimensional consistency. When χ is zero, Eqs. (6) and (13) reduce to the system governing the static response of a homogeneous linear elastic solid to imposed displacement boundary conditions. When χ takes on values greater than zero the discrete system mimics the behavior of a non-homogenous linear elastic system where the local material stiffness has been increased by a factor $(1/\Omega_e)^{\chi}$. The overall effect of this volume-based stiffening is to cause small control volumes near a moving boundary to exhibit approximately rigid body motion while exporting the bulk of the deformation to regions with larger cell sizes where deformation can be more readily tolerated without severely degrading the mesh quality.

Coding was added to Loci-STREAM to satisfy the so-called Geometric Conservation Law (GCL) which is required when solving fluid dynamics problems on generalized moving meshes. In addition, a general capability has also been implemented to specify rigid-body translation and rotation grid motions required for problems of interest in this STTR (plunging and pitching airfoils) project. In order to test the new capability, the flow about a cylinder of diameter D, oscillating in a stationary fluid has been used as a benchmark (Uzunoglu et al. 2001). The transverse motion of the cylinder is given by

$$x(t) = A\sin(\Omega t), \quad \dot{x}(t) = A\Omega\cos(\Omega t) = U_M\cos(\Omega t)$$ (2.7)
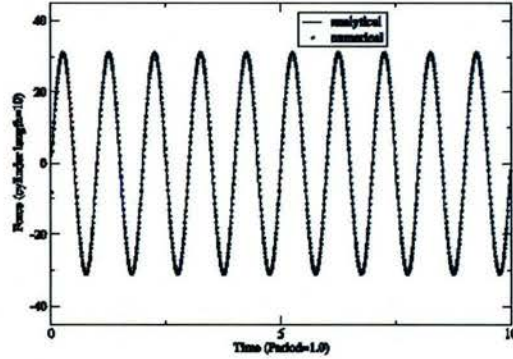
Figure 2.2-2. Inviscid force on oscillating cyinder.

where A is the amplitude of the motion and Ω is the circular frequency. For inviscid flow of small amplitude, the force per unit length acting on the cylinder is given as follows:

$$F(t) = 0.25\rho\pi D^2\ddot{x}(t)$$ (2.8)

A numerical solution was obtained with Loci-STREAM using a 61x27 grid An amplitude, A=0.1×D, was used which is considered sufficiently small to satisfy the conditions of the analytical benchmark. Figure 2.2-2 shows a comparison of the analytical and numerical solutions for ten cycles. It is clear that the numerical solution matches the benchmark extremely well.

8

2.3 Incorporation of Advanced Grid Movement Techniques

Phase I work demonstrated the feasibility of Loci-STREAM in serving as a simulation tool for flapping wing aerodynamics. Several 2-D pitching and plunging airfoil cases were investigated during Phase I work to demonstrate the need for accurate and efficient CFD capability to resolve the unsteady flow fields associated with flapping wings. To robustly and efficiently simulate the aerodynamics of flapping-wing MAVs, a robust grid movement strategy – which will not fail under conditions of extreme grid movement – is a key ingredient.

2.3.1 Rigid-Body Source Term Strategy to Reduce Grid Skewness During Movement

In our previous work (during Phase 1) it was observed that the original Stein and Tezduyar (2002) grid movement algorithm (Smith and Wright 2005), failed to produce the desired results when the so-called Jacobian-based stiffening was activated. Specifically, for cases involving rigid-body rotation of a body
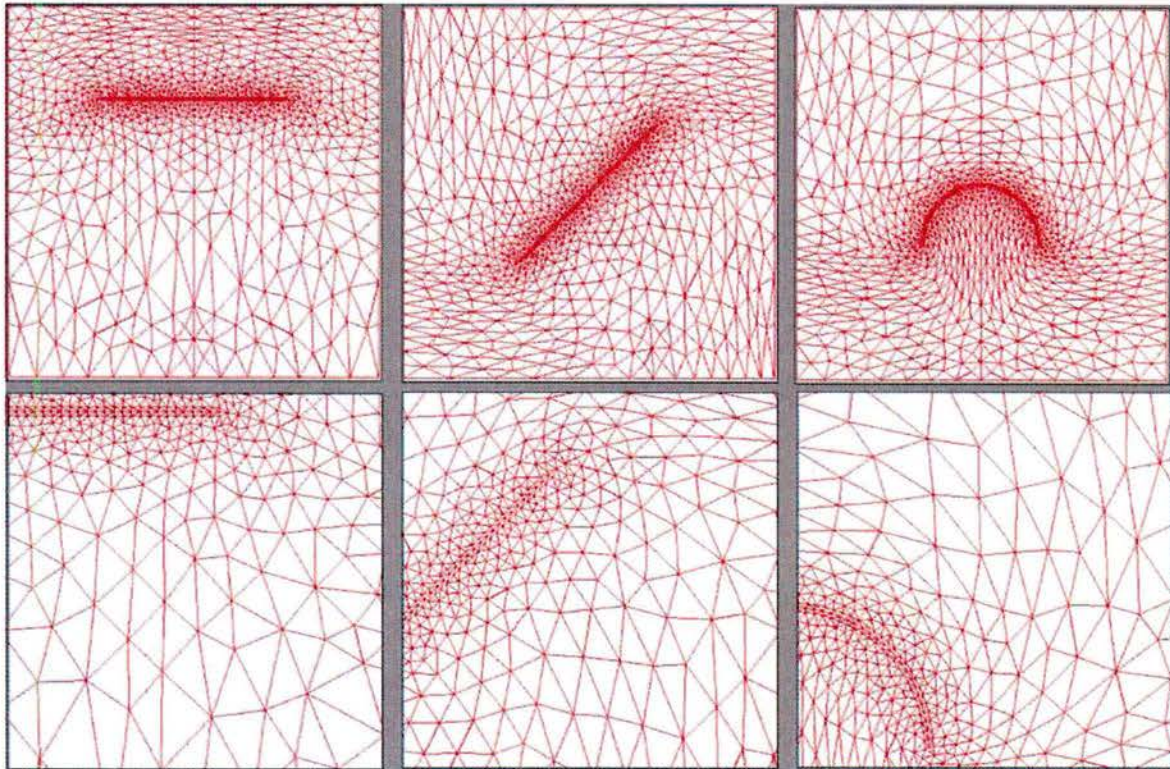
Figure 2.3-1. Results for three test cases (Stein and Tezduyar 2002) with the modified grid movement algorithm.

surface, grid lines in the vicinity of the surface failed to remain orthogonal to the surface, resulting in skewed grid elements near the surface. For large angles of rotation, correspondingly large skewness was observed, rendering the mesh essentially useless for accurate CFD calculations.

One strategy to counteract this deficiency is to use explicit rigid-body rotation for the grid nodes near a rotating surface. While this strategy is acceptable for simple two-dimensional problems, logistical problems arise for general three-dimensional cases where different parts of the surface (a flapping bird for example)

are moving in different ways, and one must identify near-surface nodes with a unique rigid-body motion. At places in the mesh such as wing-body intersections, this strategy appears to become completely intractable.

In lieu of the above approach, a simple heuristic strategy of adding a rigid-body source term to the original linear elasticity equations governing mesh movement was investigated. The source term takes the form of a diffusion flux of a modified displacement gradient tensor, in which the diagonal entries have been zeroed out, and the off-diagonal entries include the strain-free compatibility conditions. This modified source term approach is completely general, allowing its applicability to both two-dimensional and three- dimensional configurations with no algorithmic complexity. Figure 2.3-1 shows the results for the three basic Stein and Tezduyar (2002) test cases obtained with this modified algorithm. The results are essentially identical to the benchmark calculations and show a great improvement in the ability of the algorithm to maintain orthogonality of the grid lines in the vicinity of a rotating surface.

To test the new algorithm on a realistic two-dimensional configuration, a NACA0012 airfoil grid was generated, suitable for a high Reynolds number turbulence flow problem, with wall spacing of 0.0001. Figure 2.3-2 shows the deformed mesh after the airfoil has moved through 45 degrees of rotation. Only boundary node displacements have been assigned, while all internal node displacements are computed using the new mesh movement algorithm. From the far view, one cannot tell that the mesh was not explicitly rotated. The near view shows that mesh quality and near-orthogonality have been maintained even for this fine spacing near the surface of the airfoil. Overall, the new modified mesh movement algorithm appears to produce high-quality meshes even under severe boundary deformations, with robustness independent of the underlying geometry.
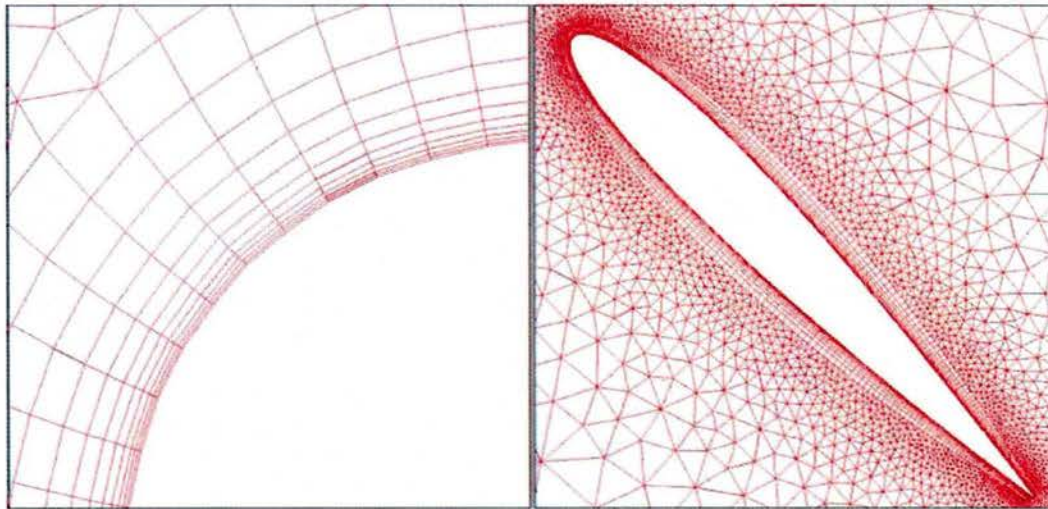
Figure 2.3-2. Deformed mesh for the NACA 0012 airfoil using the new mesh movement algorithm.

The new mesh movement strategy in Loci-STREAM was employed for flapping wing geometries presented in the following sections of this report.

2.3.2   Strategies for Grid Movement Boundary Condition Specification

One of the primary goals of the present effort was to validate Loci-STREAM with experimental data for flapping wing configurations. The experiments conducted at AFRL with the SD7003 airfoil employed a 3-D wing inside a water tunnel, with small gaps (on the order of 1mm) between the wing tips and the water tunnel walls in order to reduce 3-D effects. Since 3-D effects cannot be entirely eliminated in the water tunnel, it is important to quantify these effects so that one may understand whether deviations from experiment are caused by numerical/computational modeling issues or by differences in the experimental measurements that are actually due to 3-D effects. Thus, detailed simulations of the complete 3-D SD7003 wing in the water tunnel are required. Such computations are very challenging due to the presence of the minute gaps between the wing-tips and the tunnel walls, and a robust grid-movement strategy is essential in order to maintain grid
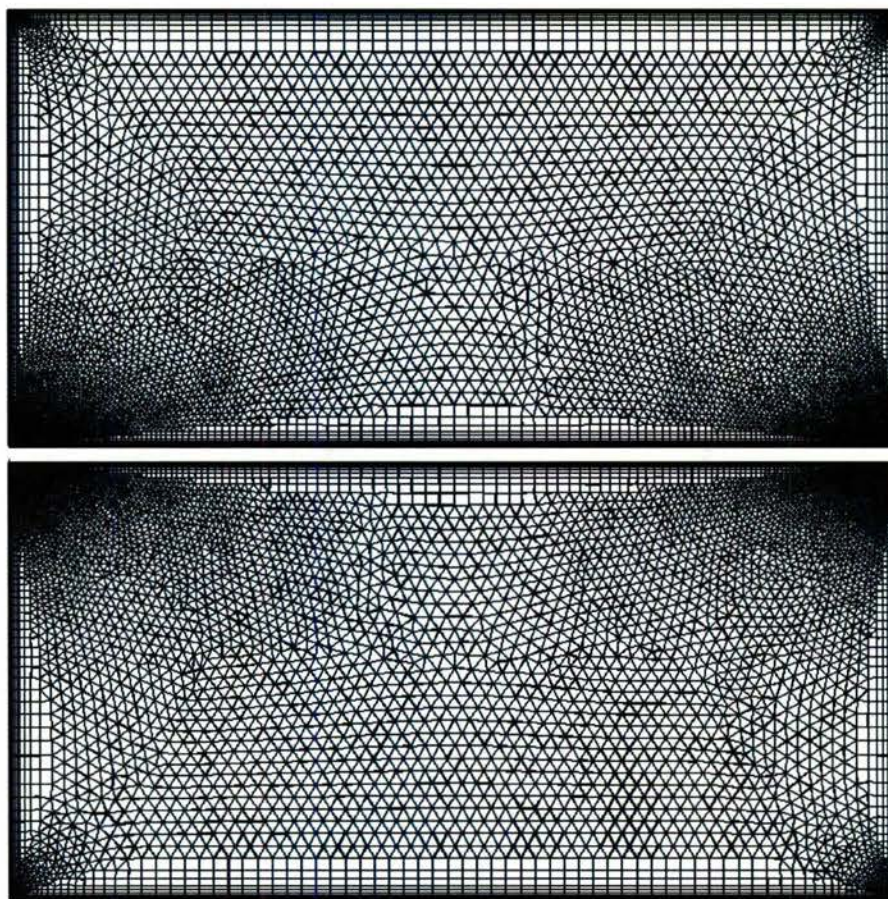
Figure 2.3-3. Global view of the computational mesh for the 2-D test problem which consists of a square of the same dimension as the water tunnel cross-section (0.61m x 0.61m) and a finite thickness plate (0.60m x 0.01m) which undergoes a periodic oscillation.

quality under the presence of relatively large wing displacements compared to gap dimensions. First, a 2-D model problem simulation was undertaken in order to:

(a) Determine if the grid generation software SolidMesh (developed at Mississippi State University) currently being used is capable of generating a high-quality mesh in the gap region which maintains appropriate boundary layer resolution while providing the proper isotropic mesh element fill between the tunnel wall and wing-tip boundary layers.

(b) Determine the best strategies for grid movement given the presence of small length-scale gaps, and

(c) Investigate if the basic grid-movement algorithm which has been developed, in conjunction with these strategies will allow us to maintain grid quality in the gap region over a period of many pitch cycles.

Figure 2.3-3 hows a global view of the computational mesh for the 2-D test problem which consists of a square of the same dimension as the water tunnel cross-section (0.61m x 0.61m) and a finite thickness plate (0.60m x 0.01m) which undergoes a periodic oscillation. The gap between the plate and the walls of the square is 0.001m which corresponds exactly to the real 3-D simulation. Figure 2.3-4 shows a blow-up of the gap region where one can see boundary layer meshes with initial spacing of 1.0e-05m growing off both the plate (wing tip) and square (tunnel wall) with isotropic cell fill-in where the boundary layers end. Other than a small region of the wall boundary layer where quadrilateral cells have been collapsed into triangles (no combination of grid-generation parameters would eliminate this), SolidMesh is clearly capable of generating the required mesh in this region.

In the experimental cases of McGowan et al. (2008) a wing of chord 0.1524m was put through a series of pure plunges with an amplitude of 5% of the chord length (0.00762m). The approximate maximum thickness of the SD7003 airfoil based on this chord length is 0.012m, which motivated the choice of a plate thickness of 0.01m. A numerical simulation was performed in which the plate undergoes an oscillation about y=0.0 of magnitude 0.01m (approximately 30% larger than actual experiment). Two strategies for specifying the boundary conditions of the grid movement were examined, and are detailed as follows:
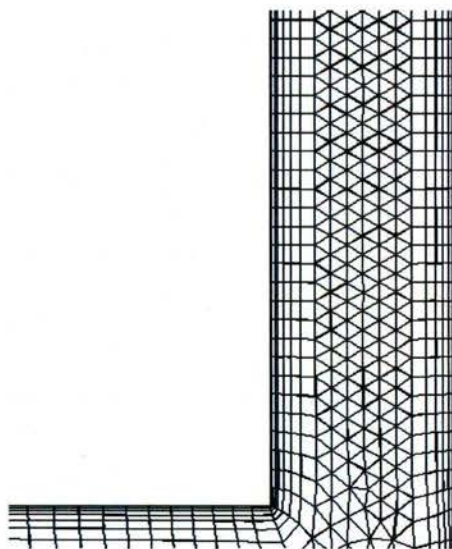

Figure 2.3-4. Blow-up of the gap region showing boundary layer meshes with initial spacing of 1.0e-05m growing off both the plate (wing tip) and square (tunnel wall) with isotropic cell fill-in where the boundary layers end.

1) The motion of grid nodes on the plate is specified with Dirichlet conditions and all other nodes are computed using the mesh movement algorithm. All wall nodes are constrained to stay in the plane of the wall.

2) Same condition for plate nodes. Boundary nodes on a small section of the tunnel wall are also prescribed to move in unison with the airfoil. All other wall nodes are computed using the mesh movement algorithm and constrained to stay in the plane of the wall.

Upon investigation of strategy 1, it quickly became apparent that the grid-movement algorithm was not capable of dragging the nodes along the wall adjacent to the airfoil in a manner sufficient to maintain adequate grid quality. This strategy was therefore abandoned. Using strategy 2, in which the adjacent wall nodes are specified to mirror the motion of the airfoil, it was found that all nodes between the wing tip and the tunnel wall move with an effective rigid-body motion which maintains the initial quality of the mesh. The simulation using strategy 2 was carried out for a total duration of four cycles at which it was terminated since it became readily apparent that no significant accumulative degradation in grid quality was occurring. Figure 2.3-5 shows a close-up of the upper part of the gap region when the plate is at its maximum positive displacement (y=0.01m) during the fourth cycle. Figure 2.3-6 shows a similar shot of the lower part the gap region when the plate is at its maximum negative displacement (y=-0.01m) during the fourth cycle. It is clear that the current grid movement algorithm (Stein and Tezduyar 2002) along with strategy 2 is very effective in maintaining excellent grid quality under amplitudes of motion of current interest. We also anticipate that these results will directly extend to the full 3-D wing simulation at comparable and even higher amplitudes of wing motion.
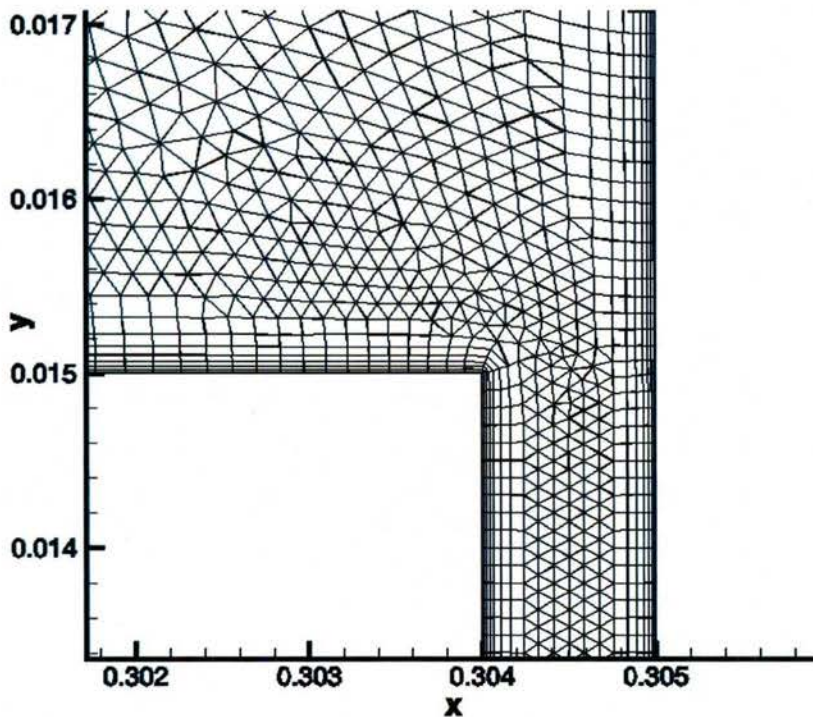
Figure 2.3-5. Close-up of the upper part of the gap region when the plate is at its maximum positive displacement (y=0.01m) during the fourth cycle.
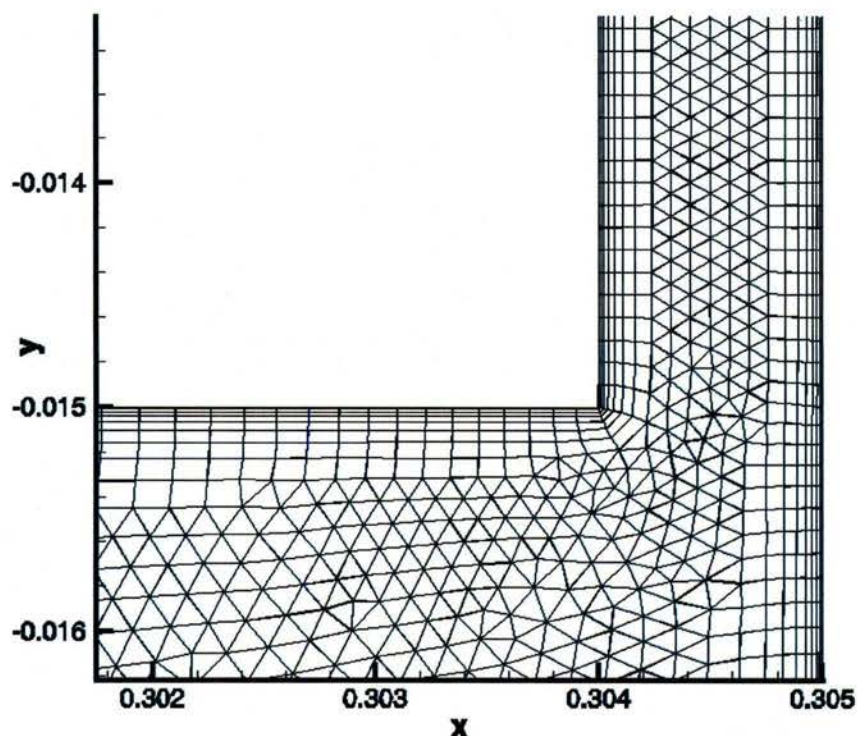
Figure 2.3-6. Lower part the gap region when the plate is at its maximum negative displacement (y=-0.01m) during the fourth cycle.

2.3.3   Investigation of Stiffness Parameter

An important part of this project in the understanding of flapping-wing flight is the use of both CFD and experiment in a symbiotic fashion to investigate the fluid-dynamic mechanisms of interest.   Initially, the CFD simulations in this project were performed for unbounded domains, with comparisons made to experimental results which have been conducted in bounded domains.   The next step in the process was to assess the impact of bounded domains on the experimental results and determine if there are any significant effects which can lead to deviations between CFD and experiment.

As a starting point in this process, a grid was generated for RTO case (1b) in the bounded domain of a water tunnel with no-slip walls both above and below the airfoil. While the top boundary is in reality a free surface, the use of no-slip boundaries above and below simulates the case in which plates have been placed on the top of the water tunnel to suppress the effects of the free surface. At a later time, the actual free-surface problem will be included in the CFD simulation. Figure 2.3-7 shows a portion of the computational domain around the airfoil near its initial configuration. The overall grid extends from an upstream position of x=-2.0 to a downstream position of x=3.0, while the lower wall lies at position y=-0.305 and the upper wall at position y=0.305. The airfoil chord is 0.1524, and the sinusoidal motion takes the airfoil a half chord length about the mean position y=0.0.

Initial investigations have concentrated on testing the grid movement algorithm over the complete range of motion of the airfoil to determine the grid movement parameters required for maintaining a quality mesh over the duration of the simulation. The primary parameter of interest in the Stein and Tezduyar (2002) grid
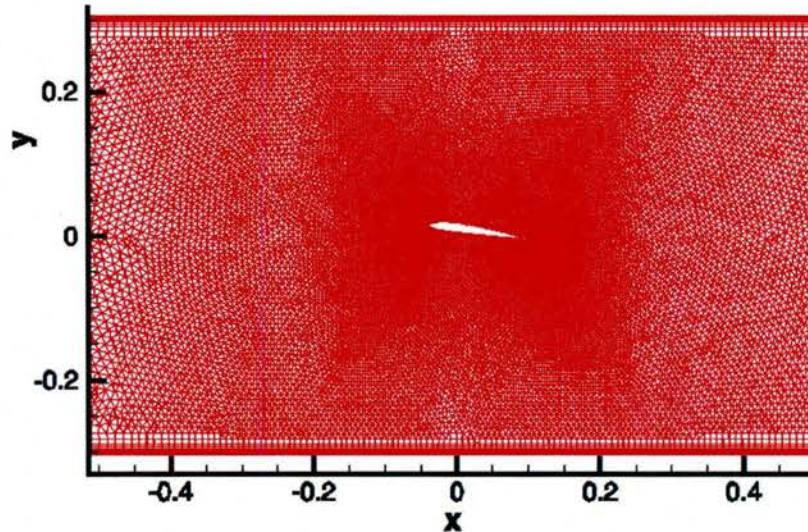

Figure 2.3-7. . Computational domain around the airfoil near its initial configuration.

movement algorithm is the stiffness parameter, which scales the size of the differential stiffness between small and large grid elements. The fundamental idea behind the algorithm is to enhance the stiffness of smaller grid elements (which tend to be near the moving body) and to relax the stiffness of larger elements (which tend to be away from the moving body).

For moving mesh cases with unbounded domains, relatively large values of the stiffness parameter χ can be used. This results in a mesh which is nearly rigid in the vicinity of the moving body, while allowing significant mesh deformation to occur far away from the body in order to accommodate large physical displacements of the moving body while suffering virtually no loss in grid quality at any location in the domain. For the current bounded domain case, initial investigations have shown that much smaller values of the stiffness parameter must be used in order to maintain adequate grid quality.

Figure 2.3-8 (a,b,c) show portions of the CFD mesh for $\chi=1.5$ when the airfoil is located at its maximum vertical displacement. For this relatively large value of the stiffness parameter, the grid quality in the vicinity of the leading and trailing edges of the airfoil is seen to be excellent, virtually the same quality as the initial configuration. Near the lower wall however, the mesh has undergone what appears to be a delamination process, resulting in an unacceptable mesh at this point in the airfoil displacement cycle. This breakdown in the mesh is essentially caused by too high a stiffness parameter, in which case there are no pliable elements that are able to distort and thus allow for a smooth variation of mesh displacement.

Figure 2.3-9 (a,b,c) shows the same portions of the mesh for $\chi=0.8$ which is an intermediate value of the stiffness parameter ($0.0<\chi<2.0$). The close-ups of the mesh in the vicinity of the leading and trailing edge show that while the mesh is not as high a quality as for $\chi=1.5$, it is of sufficient quality as to allow an accurate solution. In addition, the lower stiffness parameter value has allowed larger grid elements between the airfoil and the lower wall to distort in a smooth fashion, thus preventing the delamination phenomenon associated with the higher stiffness parameter.

15
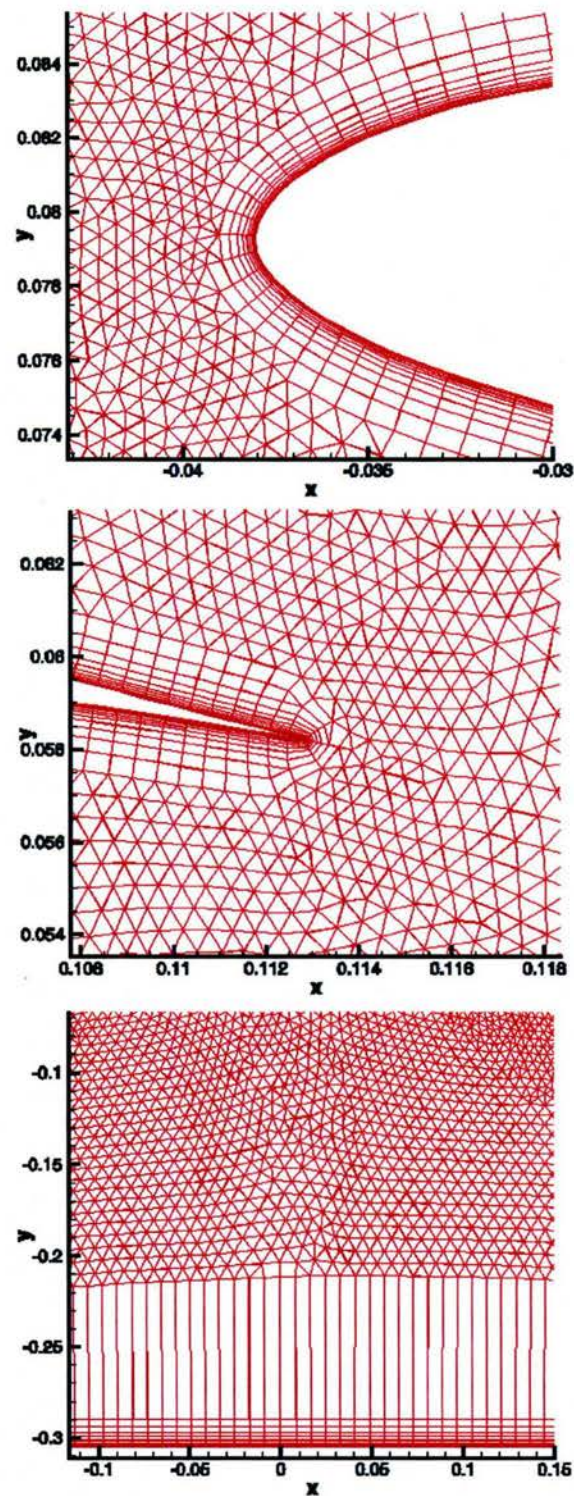
Figure 2.3-8. Grid for χ=1.5 when the airfoil is located at its maximum vertical displacement.
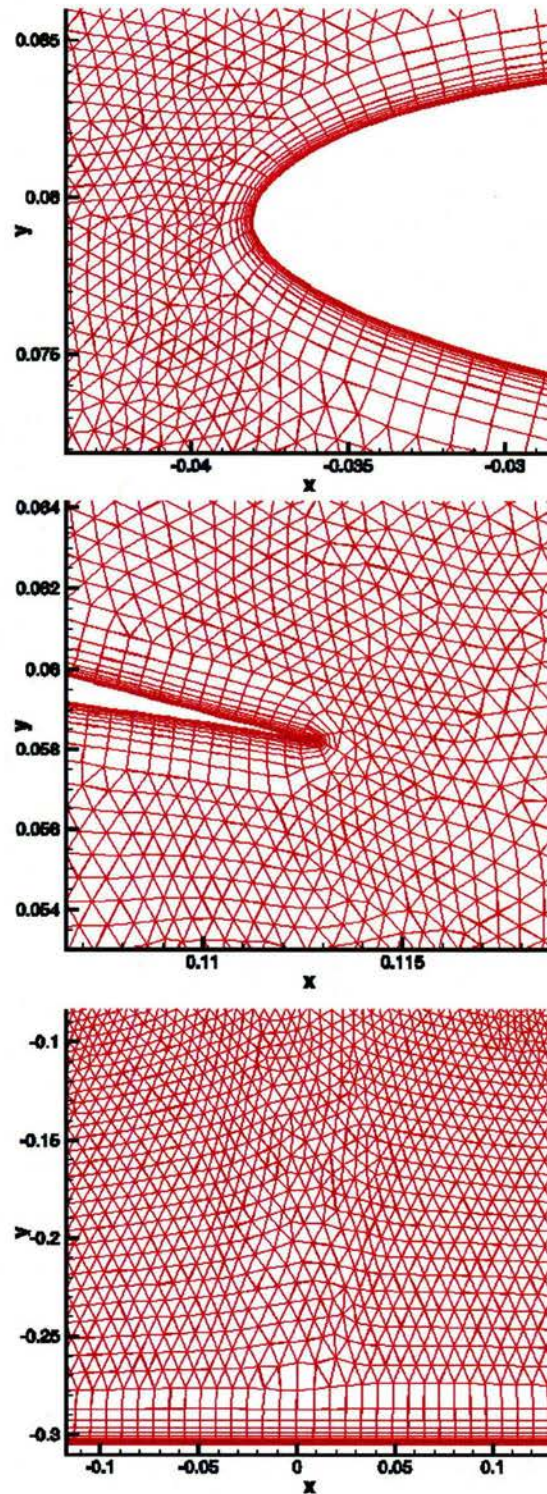
Figure 2.3-9. Grid for χ=0.8 when the airfoil is located at its maximum vertical displacement.

2.4 Validation of Loci-STREAM with Experimental Data for Pure Plunging SD7003 Airfoil

Experimental data (McGowan et al. 2008) involving phase-averaged measurements using particle image velocimetry in a water tunnel was used to validate the Loci-STREAM code for an oscillating SD7003 airfoil in the pure-pitch mode. Reynolds numbers of 10,000 and 40,000 (based on free stream velocity and airfoil chord) were selected as representative values for, respectively, a situation where transition would not occur, and a situation where transition in attached boundary layers would be of some significance. The plunging motion is at the reduced frequency of k=3.93 with the pivot point at the quarter chord. The computational and experimental results are plotted side-by-side in Figure 2.4-1 and Figure 2.4-2 for Re=10,000 and in Figure 2.4-3 and Figure 2.4-4 for Re=40,000. Contours of streamwise velocity (non-dimensionalized by the free stream velocity) are plotted in Figure 2.4-1 and Figure 2.4-3. Contours of vorticity (non-dimensionalized by free stream velocity and airfoil chord) are plotted in Figure 2.4-3 and Figure 2.4-4. The contours are plotted at four different phases at which the data was taken, namely, the beginning of the cycle, ¼ of the cycle, ½ of the cycle, and ¾ of the cycle.
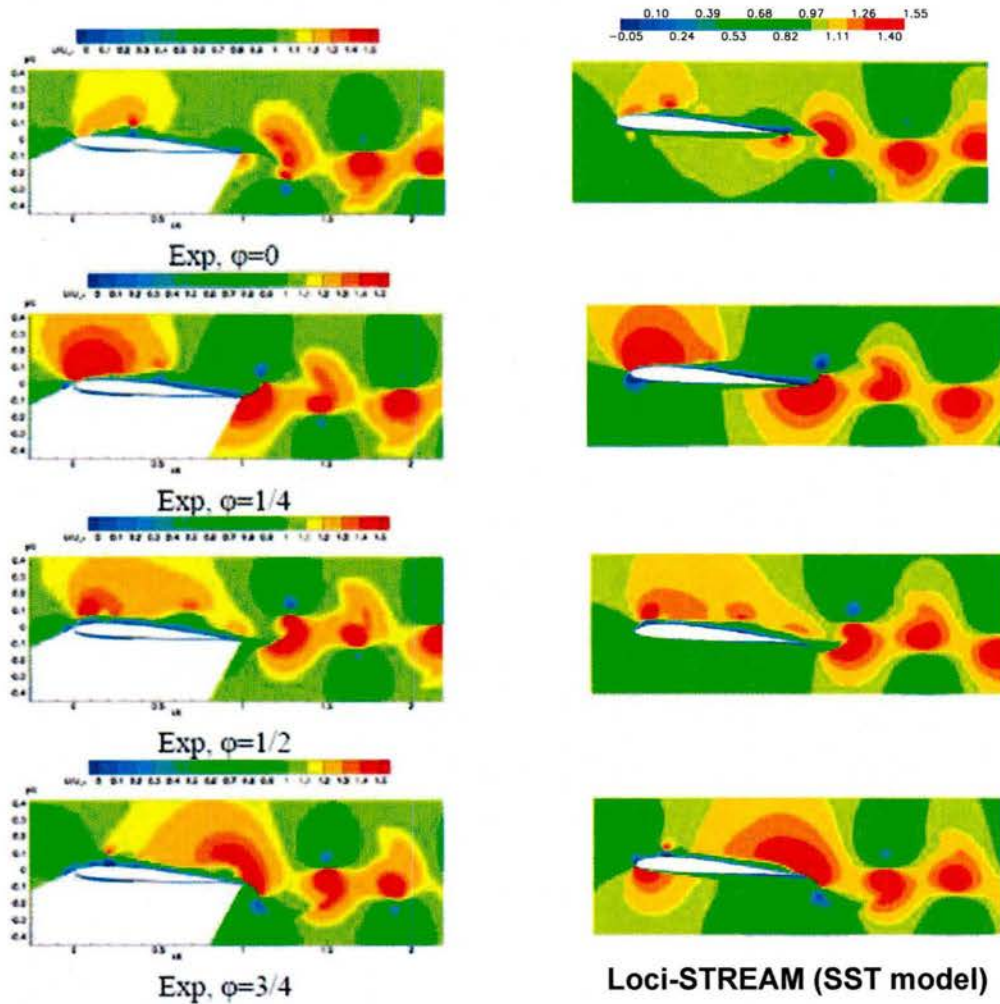
Figure 2.4-1. SD7003 airfoil; pure plunge; Re=10,000. Streamwise velocity.
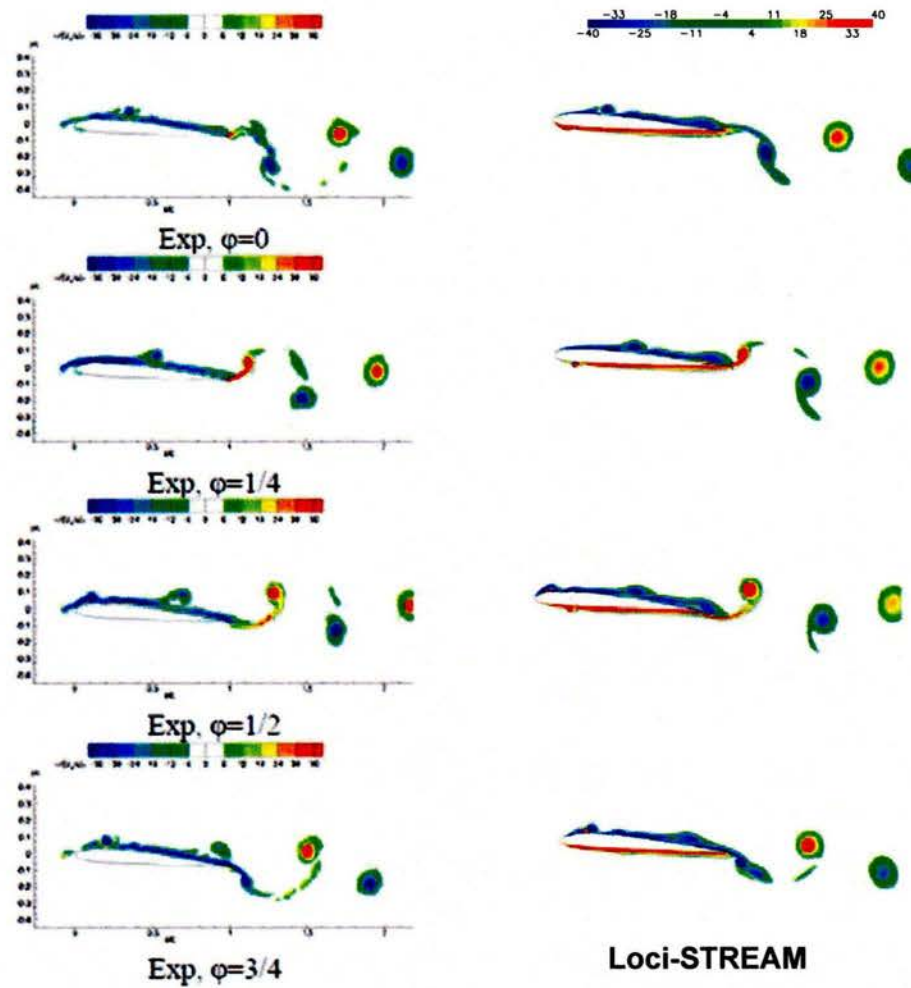
Figure 2.4-2. SD7003 airfoil; pure plunge; Re=10,000. Vorticity.
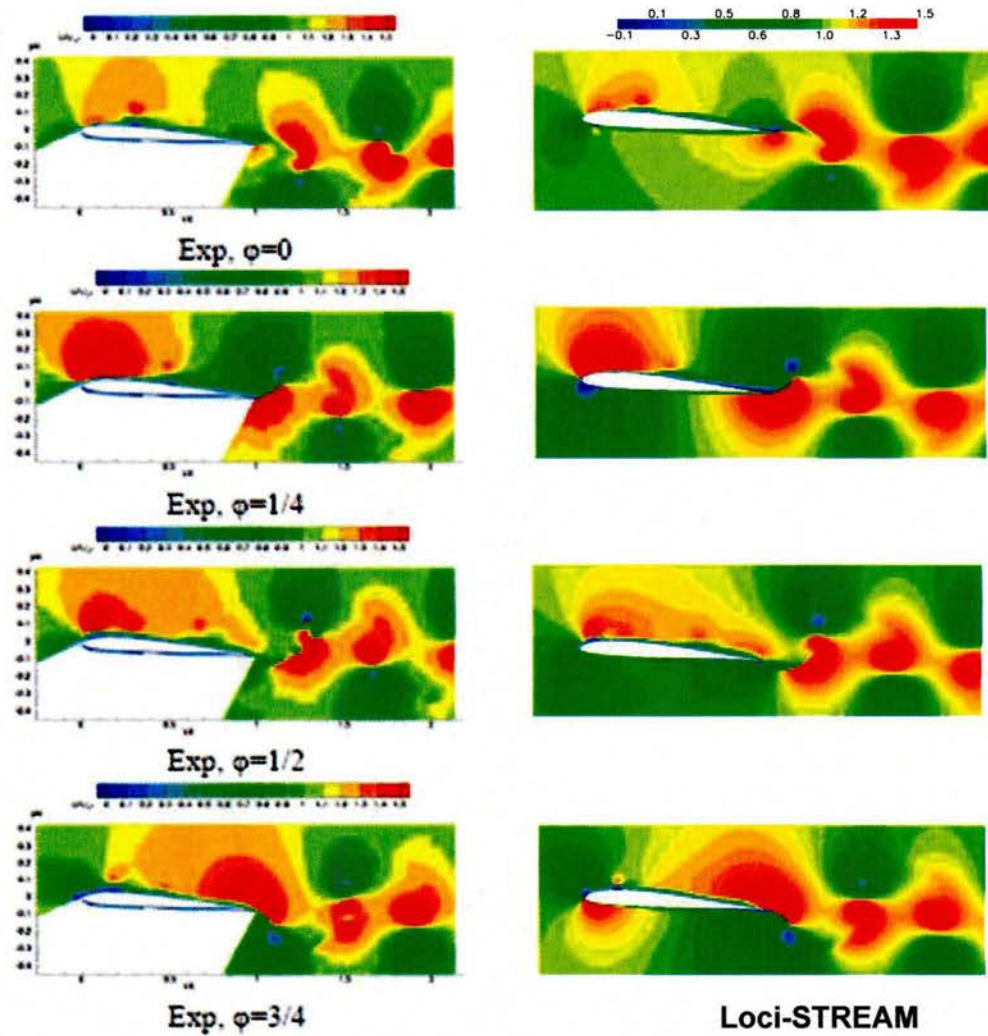
Figure 2.4-3. SD7003 airfoil; pure plunge; Re=40,000. Streamwise velocity.

3

Figure 4. SD7003 airfoil; pure plunge; Re=40,000. Vorticity.

Exp, φ=0

Exp, φ=1/4

Exp, φ=1/2

Exp, φ=3/4

Loci-STREAM
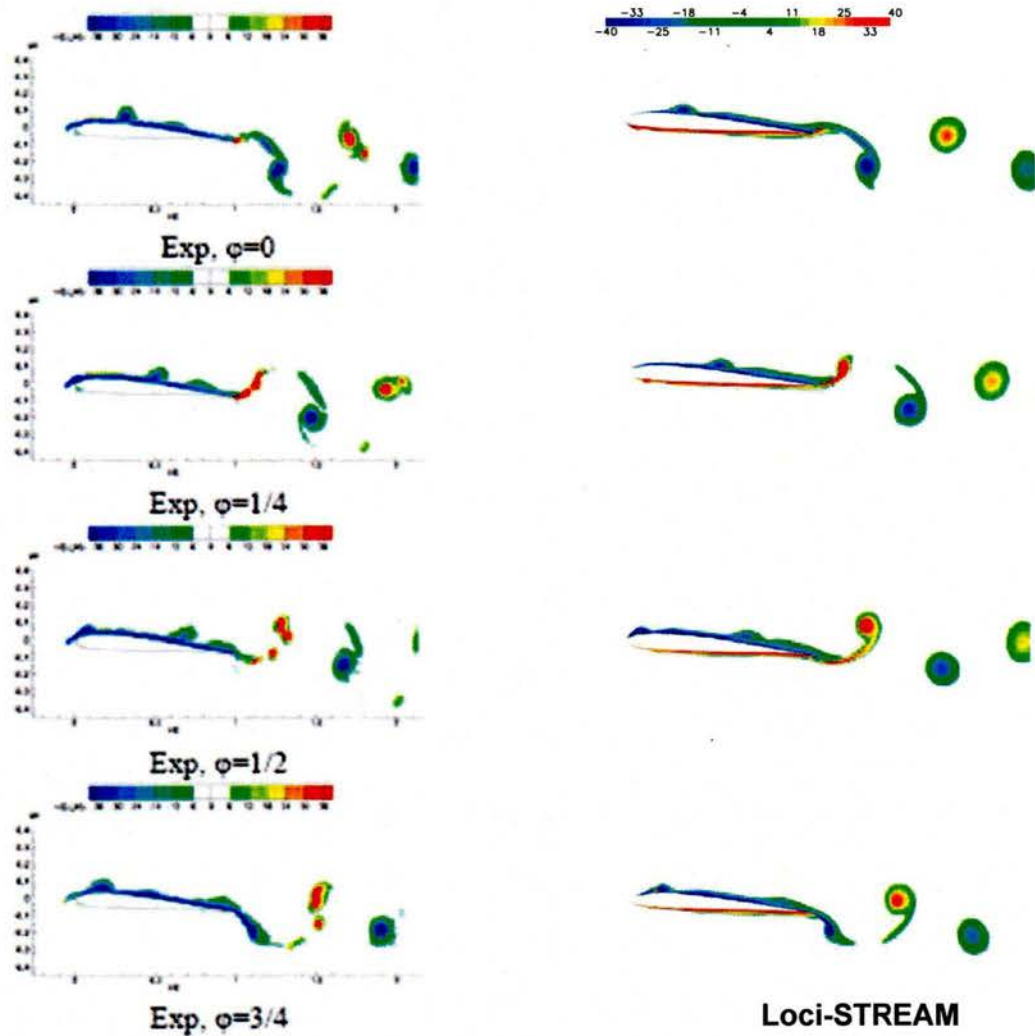
Figure 2.4-4. SD7003 airfoil; pure plunge; Re=40,000. Streamwise velocity.

The agreement between the computation and the experiment is very good. The computations accurately capture the strong shear layer that develops near the trailing edge during the plunge motion. The vorticity results from the Loci-STREAM code show its capacity to adequately resolve shed vortical structures near the airfoil and in the wake.

2.5   Development of an Optimization Framework

In order to create an effective tool for the design of MAVs, the basic fluid-structure solver must be coupled with an optimization strategy. While the fluid-structure solver can provide detailed information about the flow physics of a particular MAV configuration under any given flight conditions, a complete parametric study involving numerous configurations with multiple flight conditions must be conducted in order to determine the potential "best design" for an MAV. Given the current state of computing power, primarily in regards to unsteady simulations over complex 3-D geometries, one must find a way to determine the sensitivity of the design to the input parameters while conducting the minimum number of CFD simulations. An effective optimization strategy can reduce, by orders of magnitude, the number of simulations required for the complete characterization of the design with respect to geometric and flow parameters. Development of an optimization framework was a key element of Phase 2 work.

While the ultimate goal of this effort is to seek the 3D kinematics yielding the best performance for flapping wings with varying sizes, frequency, structural complexity, and capable of handling forward flight, hovering and wind gust scenarios, the task presented in this section deals with a better understanding of the interaction and effects of the unsteady flow mechanisms and comparing potential kinematic combinations with the use of surrogate models. Reynolds number effects have been examined previously, and one such consequence, the asymmetric forward and back stroke, is seen as a consequence of interactions with the jet like flow feature. The sinusoidal hovering kinematics utilized here been used in former studies as well, and yet there are still questions even in the simplified 2D domain. What constitutes "good" kinematics? This is a context specific question, e.g., the measure of merit may be lift, but then the next relevant question is why, and at what cost (power consumption). Why are certain combinations of variables better than others and can any general trends be stated? This is merely a starting point. After a stronger foundation has been set other aspects can be addressed. Transitional effects are relevant at Reynolds numbers seen by MAVs and are one of the open challenges in the field. The 3D effects at relatively low aspect ratios are quite important. The traditional wing tip vortices are present but there are also highly complex flow field interactions which can be seen in computations of a flapping hawk moth. All of these are possible avenues that can be eventually integrated into the current framework.

Surrogate modeling is one of the optimization methodologies used in engineering environments. Queipo et al. (2005) present an overview and highlights the strengths and issues in using surrogate based analysis while Goel et al. (2006) specifically address shortcomings of the experimental designs. Surrogate modeling provides an efficient method for mining information from limited data sets which is usually expensive, be it in computational or experimental costs. Examples of engineering applications include shape optimization using response surfaces as well as other surrogate models in the design of rocket injectors and supersonic turbines (Shyy et al. 2001). It is seen that alternatives to gradient based optimizations are needed, and these examples provide empirical evidence of the utility in using surrogate models. In the present study, they are used to get an idea of how the design space behaves away from the known data points. Not only does this help clarify the general trends, but when the design of experiment (DOE) is done properly, the result is more efficient use of computational resources.

2.5.1   Theodorsen's Solution

Theodorsen (1935, 1942), is able to separate the instantaneous and delayed reactions of an incompressible fluid caused by an unsteady body. The assumptions include potential flow, small oscillations, and thin airfoil simplifications. Furthermore, a Kutta condition is imposed on the trailing edge, and a planar wake is assumed. This means that, strictly speaking, this solution doesn't include the effects of vortex roll-up, shedding, as well as open separations. For pitch, and plunge described as $\alpha(t) = \alpha_a e^{i(\omega t + 2\pi\phi)}$ and

$h(t) = h_a e^{i(\omega t + 2\pi\phi)}$ $h(t) = h_a e^{i(\omega t + 2\pi\phi)}$, respectively, the lift is predicted as

$$L = \pi\rho b^2 \left[\dot{h} + U_\infty \dot{\alpha} - ba\ddot{\alpha} \right] + 2\pi\rho U_\infty b C(k) \left[\dot{h} + U_\infty \alpha + b\left(\frac{1}{2} - \alpha\right)\dot{\alpha} \right], \tag{2.9}$$

where b is semichord length, U_∞ is the freestream velocity, k is the reduced frequency defined as $k = \dfrac{\omega b}{U_\infty}$

$k = \dfrac{\omega b}{U_\infty}$, and $C(k)$ is the Theodorsen's lift deficiency function. The Theodorsen's lift deficiency function is a complex function which can be expressed using Hankel functions of first and second kind. Furthermore, if there is a constant initial angle of attack, then this steady-state contribution can be superimposed to Eq. (2.9).

The first term in Eq. (2.9) is referred as the added mass term. This term gives the instantaneous reaction of the flow to the airfoil motion, and the resulting pressure distribution. The second term, the circulatory term, that contains the Theodorsen's lift deficiency function, represents the influence of the wake vortices. Since the magnitude $C(k)$ is always less than unity, this circulatory term brings reduction in the lift amplitude, and also phase lag into the flow.

Two particularly useful approximations to the above form are the steady-state,

$$L = 2\pi\rho U_\infty b \left[\dot{h} + U_\infty \alpha \right], \tag{2.10}$$

and quasi-steady approximations,

$$L = \pi\rho b^2 \left[\dot{h} + U_\infty \dot{\alpha} - ba\ddot{\alpha} \right] + 2\pi\rho U_\infty b \left[\dot{h} + U_\infty \alpha + b\left(\frac{1}{2} - \alpha\right)\dot{\alpha} \right], \tag{2.11}$$

For the steady-state case, we have the steady-state formula except that the angle of attack has been replaced by the effective angle of attack. In the quasi-steady approximation, C(k) → 1 as k → 0, and the impact of the shed vortices is ignored.

2.5.2   Surrogate Modeling

The surrogate modeling techniques are used to gain a better understanding of the impact of the design variables. The various time histories give a telling story as to what is happening for each combination, but illustrating the overall impact is not straight forward, even when limited to three degrees of freedom. Surrogate modeling provides a way to stand back from the trees and see the forest if you will. The process is split into three main parts. The first is constructing the design of experiment (DOE), or method for choosing how many and for which points to run full CFD simulations. These then provide the necessary data for the fitting of the surrogate models which can be used to approximate a quantity of choice at arbitrary points within the design space. The third piece of the process is a sensitivity analysis which can be used to quantify the importance of each design variable, and in some cases eliminate them from consequent refinement iterations.

2.5.3   Design of Experiment (DOE)

The DOE used a face centered cubic design (FCCD) (Shyy et al. 2001) and then Latin hypercube sampling (LHS) (Queipo et al. 2005) to appropriately fill in the remainder of the design space. A 2nd order polynomial response surface construction has (N+1)(N+2)/2 coefficients, N being the number of variables, and in general, one wants twice this many data points for a proper curve fit. A FCCD design provides 2^N+2N+1 points: 2^N corner points, 2N face points, and one center point. Thus for three design variables, FCCD provides 15 of the 20 points required. The LHS then provides a method for efficiently choosing the rest of the points by maximizing the distance between the added points, though by no means is it the only alternative (Queipo et al. 2005).

2.5.4 Composite Surrogates

Which surrogate model(s) to use is an interesting challenge in and of itself. The current approach utilizes the current state of the art work of Viana et al. (2008). Here a number of different surrogate models are constructed and are evaluated based on their respective cross-validation errors, namely PRESS. In this fashion no extra test points are needed, rather the models are constructed with one less training point and the deviation of this point from the constructed surrogate is used calculate one component of the PRESS. Each of the training points is treated in a similar manor and one can subsequently quantify how well the respective surrogate model fits. As Viana et al. (2008) illustrates for problems in lower dimensions, using the best PRESS surrogate model might be justified, whereas in higher dimensions it is much riskier to do so.

The current setup evaluates Kriging (Queipo et al. 2005), 2nd order polynomial response (PRS) (Myers and Montgomery 2002), radial basis neural network (RBNN) (Cheng and Titterington 1994), and 6 support vector regression (SVR) (Smola and Scholkopf 2004) models noted in Table 2.5-1 below. The two best models in the current context, as measured by those exhibiting the lowest PRESS values, are the SVR model using a full spline kernel and Kriging.

Table 2.5-1. Defining surrogate model traits.

Model	Comment 1	Comment 2
Kriging	Linear Regression Model	Gaussian Correlation Model
PRS	2nd Order Polynomial	-----
RBNN	Max Neurons = 1000	-----
SVR1	Linear Spline Kernel	Full- infinity as upper bound (non-separable case)
SVR2	Linear Spline Kernel	Short- finite upper bound
SVR3	Exponential Kernel	Full
SVR4	Exponential Kernel	Short
SVR5	Gaussian Kernel	Full
SVR6	Gaussian Kernel	Short

2.5.5 Global Sensitivity Analysis

The global sensitivity analysis is in general useful for: (i) Determining if a variable is particularly influential in the design space, if not perhaps the variable can be fixed and the degrees of freedom and complexity of the problem reduced. (ii) Ranking the importance of the design variables. (iii) Quantifying the degree of coupling between design variables. For example, is the influence on the design space mostly an individual effort, or is there an effect caused by the interaction of variables?

Sobol's method (Sobol 1993) is used to for the global sensitivity evaluations. The surrogate model can be written as:

$$f(x) = f_0 + \sum_i f_i(x_i) + \sum_{i<j} f_{ij}(x_i, x_j) + \ldots,$$ (2.12)

Once this decomposition has been calculated the total variance,

$$D = \int f(x)^2 dx - f_0^2,$$ (2.13)

24

and partial variances, e.g.,

$$D_1 = \int f_1(x)^2 dx_1 dx_2 dx_3, \qquad (2.14)$$

can be calculated. In this fashion, individual contributions, such as D_1/D, or combinations of variables, e.g., D_{12}/D, can be quantified, effectively capturing the sensitivity of the variable(s) under consideration.

2.5.6   Elliptical Airfoil

A plunging and pitching airfoil was used for this purpose. The translational and rotational airfoil motions are dictated by Eqs. (2.15) and (2.16):

$$h(t) = h_a \sin(2\pi f t), \qquad (2.15)$$

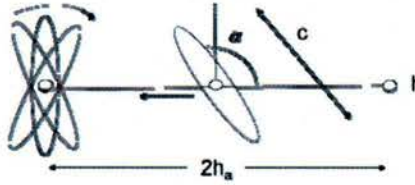$$\alpha(t) = \alpha_0 - \alpha_a \sin(2\pi f t + \phi). \qquad (2.16)$$

Figure 2.5-1. Illustration of the kinematic parameters for normal hovering.

Here $h(t)$ and h_a are the translational position and plunging amplitude respectively (see Figure 2.5-1). The angular orientation, initial angle, and angular amplitude are $\alpha(t)$, α_0, and α_a. The pitching is about the center of the rigid airfoil; this is an ellipse having a 15% thickness for all cases under consideration. The phase lag between the two motions is φ, and the frequency is denoted f whereas the time is again t. While there are a few choices in how to accommodate these kinematics computationally, the current implementation forces the grid to rotate and translate with airfoil. The geometric conservation law (GCL), a necessary consideration in domains with moving boundaries, is satisfied. The boundary condition applied to all outer boundaries is the incompressible inlet with density and velocity specified.

Due to the kinematic constraints there are only two relevant non-dimensional groups in the incompressible case. The Reynolds number is given by

$$\mathrm{Re} = \frac{U_{ref} L_{ref}}{v} = \frac{(2\pi f h_a) c}{v}, \qquad (2.17)$$

and the plunging amplitude to chord ratio is given by

$$\frac{2h_a}{c}. \qquad (2.18)$$

The reduced frequency is given by

$$k = \frac{2\pi L_{ref}}{2U_{ref}} = \frac{2\pi f c}{2(2\pi f h_a)} = \frac{c}{2h_a}. \qquad (2.19)$$

One can see that the reduced frequency, k expressed in Eq. (2.19), contains the same information as the plunging ratio. Note that since the Reynolds number is held constant, where the reference velocity and length are taken to be the maximum translational velocity and the chord length respectively, h_a and f are not independent. The three quantities that can vary are h_a, α_a, and φ. For the compressible case the Mach number is also relevant.

2.5.6.1 Design Space

The range of the variables was chosen based on the works of Weis-Fogh (1973) and Ellington (1999), which tabulated actual measurements from various species, some of which are reproduced in Table 2.5-2. The bounds for the simulations are listed in Table 2.5-3, though it is worth noting that $\varphi < 90°$, also referred to as delayed rotation, is not expected to be found in nature for hovering flight as the airfoil is flying upside for portions of the cycle. These cases were included to provide some symmetry for the other extreme, $\varphi > 90°$ or advanced rotation. Furthermore, measurements regarding α_a are also difficult to come by, though comments found in Ellington (1999) would imply that the choice of bounds, Table 2.5-3, for this variable are reasonable.

	c (cm)	f (Hz)	$2h_a/c$	Re_{wing}
Fruit Fly: Drosophila virilis	0.15	240	3.5	250
Honey Bee: Apis mellifica	0.43	240	2.8	1900
Bumble Bee: Bombus terrestris	0.73	156	2.8	4800
Hummingbird: Archilochus colubris	1.5	52	3.6	6400
Hawkmoth: Manduca Sexta	2.5	27.3	2.6	6700
Hummingbird: Patagona gigas	4.3	15	3.6	15000

Table 2.5-2. Selected data on the time and length scales encountered in nature. The examples listed do not provide upper or lower bounds for any of the categories listed, but do provide a window which captures many of the insects and animals capable of hovering flight.

Parameter	Minimum	Maximum
$2h_a/c$	2.0	4.0
α_a	45°	80°
Φ	60°	120°

Table 2.5-3. Minimum and maximum values of the plunging ratio, angular amplitude, and phase lag simulated in the surrogate modeling exercise.

To balance the computational expense these simulations were carried out on an 81x81 grid, a resolution which was not grid independent, but captured the relevant behavior immediately surrounding the airfoil fairly well.

2.5.6.2 Force Interpretation

To better understand the implications and limitations of the surrogate modeling results an example is presented of a representative normal hovering case at a Re of 100 (Figure 2.5-2). The objective functions for these cases will be the time integrated C_L and an approximation to the non-dimensional time averaged power

required which is calculated by multiplying the non-dimensional translational velocity by the C_D.

The discussion following is generally applicable to the cases where Φ=90, with slight modifications. For cases where the phase lag dictates advanced rotation ($\Phi > 90$) or delayed rotation ($\Phi < 90$), the same ideas can be extended though, like the parameter suggests, the translation and rotation will be out of phase. The cycle can be broken up into three overlapping regions defined by the unsteady flow mechanisms present. The first region starts at point 1, once again referring to Figure 2.5-2, which is near a local minimum in the lift. As the airfoil is vertical at this point, one would generally expect zero lift. As time continues the airfoil turns back into its previous trajectory which is commonly referred to as wake capturing, points 1, 2, and 3. The peak seen at point 3 will be referred to as the wake capturing peak. Flow field snapshots of vorticity (Figure 2.5-3), demonstrate the nomenclature more clearly.
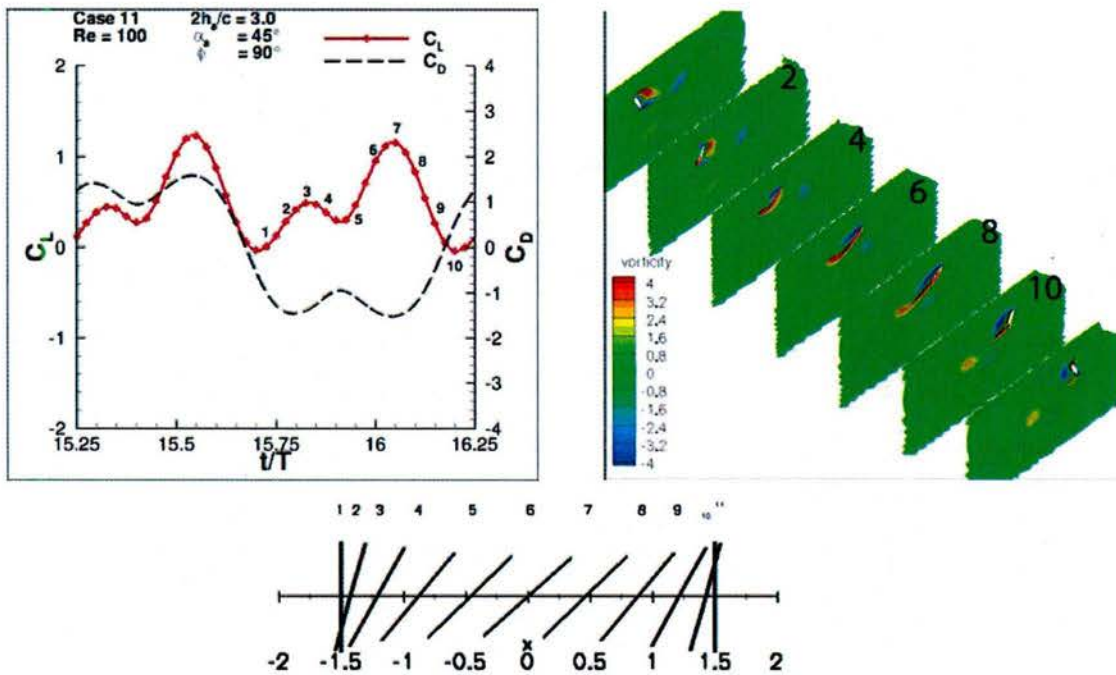

Figure 2.5-2. Illustration of the force histories over a normal hovering cycle for the parameters of $2h_a/c = 3.0$, $\alpha_a = 45$, and Φ=90 and the corresponding airfoil positions.
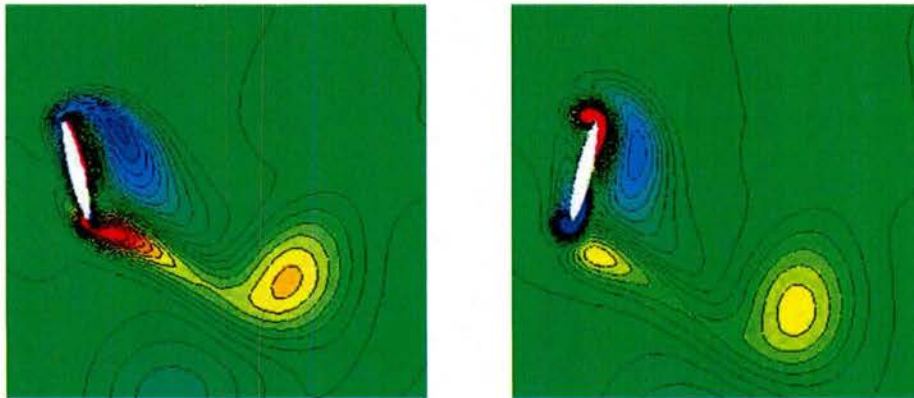
Figure 2.5-3. Illustration of vorticity countours (red: clockwise, blue counter-clockwise) and the wake capturing portion of the cycle where the airfoil turns back onto its wake possibly taking advantage of the unsteady aerodynamics. In Figure 2.5-2, these plots would correspond to points on either side of point 1. The unlabelled point 0 on the left which belongs to the end of the backstroke, and point 2 on the right.

The second and third unsteady flow features overlap significantly. The most commonly known is the delayed stall phenomenon which is generally associated with a leading edge vortex (Figure 2.5-4). Here a vortex forms behind the leading edge of the airfoil, causing a low pressure region and enhancing lift. Note that in the case illustrated, higher lift is achieved at angles of attack of 45 degrees, an angle well beyond the steady state stall. In cases with higher angular amplitudes, and therefore lower angles of attack, the peak at points 7 and 8 can be reduced significantly because the orientation of the airfoil is not able to promote LEV formation.
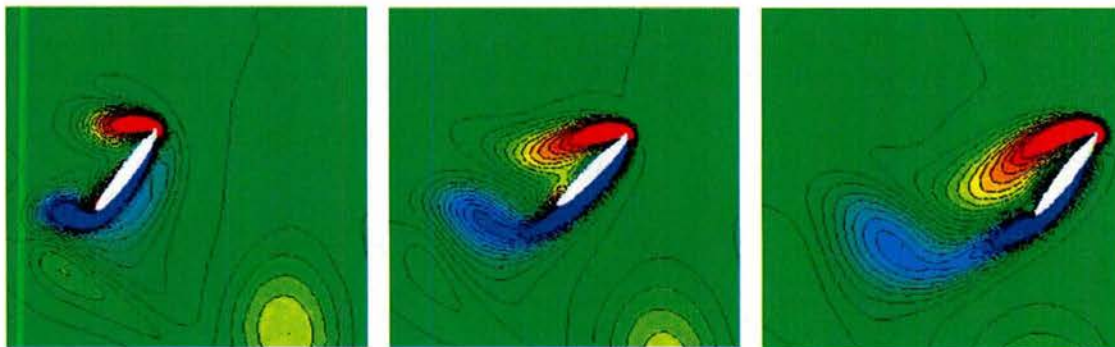

Figure 2.5-4. Illustration of unsteady delayed stall mechanism and the LEV with vorticity countours (red: clockwise, blue: counter-clockwise) In Figure 2.5-2, these snapshots correspond to points 4, 6, and 8 respectively.

Figure 2.5-5. Illustration of the jet flow feature which develops in the path of the airfoil. Velocity contours are displayed (red: positive, blue: negative) with select percentages of the maximum translational velocity marked. In Figure 4 these snapshots would correspond to points 2 , 6, and 10 respectively.

The last unsteady flow mechanism is a jet-like flow feature (see Figure 2.5-5) present in the path of the airfoil where a persistent downward velocity develops. These regions within the jet are of comparable magnitude to the maximum translational velocity of the airfoil itself and are influential for a large segment of the cycle, in this case roughly from point 4 to point 9. This jet is the cause of the asymmetry seen between forward and backstrokes (see Figure 2.5-3), and is due to the fact that the jet is slightly off centered in the direction in which the motion was started. The jet also explains the local minimum, near point 5. If the angle of attack is low (higher angular amplitudes), or the jet strength is stronger (shorter plunging amplitudes mean the jet decays less between encounters) then this wake valley will become deeper. To help convince the reader of the jet's influence C_L has been plotted during the first two cycles as well as the 15th cycle where the differences between previous cycles has largely stopped at the spatial and temporal resolutions used (Figure 2.5-3). Note that because the simulation starts with a large discontinuity in airfoil velocity, and the plots are shifted such that the force histories start when the airfoil is at the end of its translation, the 1st cycle does not imply no wake. Rather it serves to provide credibility to the claim that the jet is at least partly responsible for the aerodynamic performance recorded (i.e. the LEV is not the only factor) as it is clear that as the jet changes strength, the aerodynamic characteristics respond in a noticeable fashion.
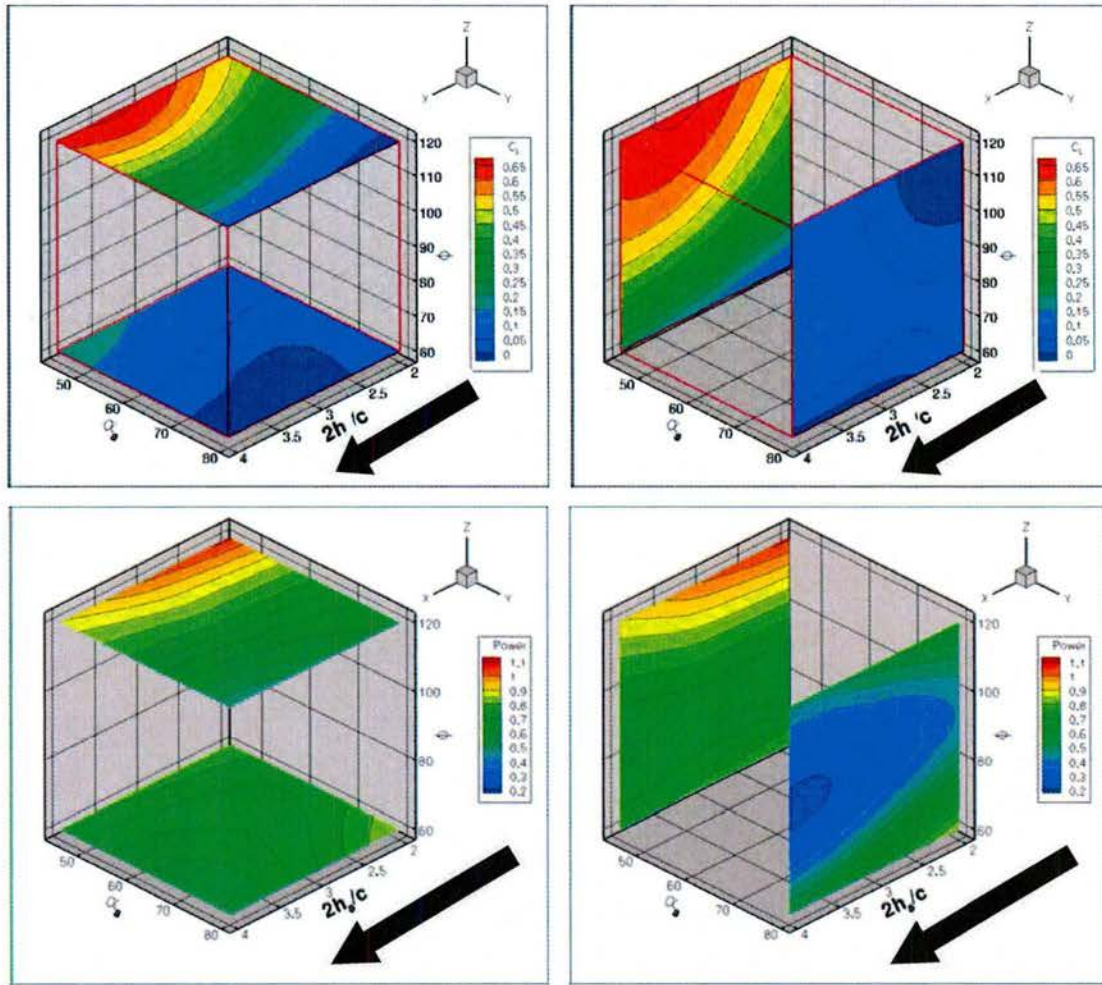
Figure 2.5-6. The lift coefficient (top) and power required (bottom) as approximated by the WAS illustrating the effect of the plunging amplitude. For the integrated effect over the entire cycle it is seen that this is the least sensitive of the design variables. Arrows show the direction of increasing plunging amplitude.

2.5.6.3 Kinematics

Plunging Amplitude

Somewhat surprisingly, the plunging amplitude, and with it the reduced frequency, had the smallest influence on lift and the required power throughout the study. Since the peak translational velocity of the airfoil is equal for all cases, the fact that the plunging amplitude has little effect on the power required per cycle is to be expected. However, the effect on lift of the unsteady flow mechanisms is less easily predicted as is their cumulative impact. It is readily apparent from the surrogate response of the design space, as seen by the small gradients found in the direction of the arrows in Figure 2.5-6, that the plunging amplitude's influence is limited.

To gain a more comprehensive look on the plunging amplitude's influence, three force histories are shown in Figure 2.5-7. The first observation is that the wake capturing peak is slightly smaller as the plunging amplitude is increased. The most significant change though is in the wake valley. The valley is the deepest when the plunging amplitude is short. As the plunging amplitude increases, the intensity of the jet found in the wake is able to decay before interaction with the airfoil. The influence of the jet is detrimental to the lift under these conditions, and a weaker jet corresponds to a higher lift for airfoils at identical angles of attack and translational velocities. Moving on to the delayed stall peak, seen as the global maximums, there is little influence on the peak amplitude. The general implication then is to minimize the negative impact the persistent jet has after the wake capturing peak. In the context of plunging amplitude this means increasing the stroke length to encounter a weaker jet, or looking at it from another perspective this could be seen as approaching jets of similar intensity at higher angles of attack.
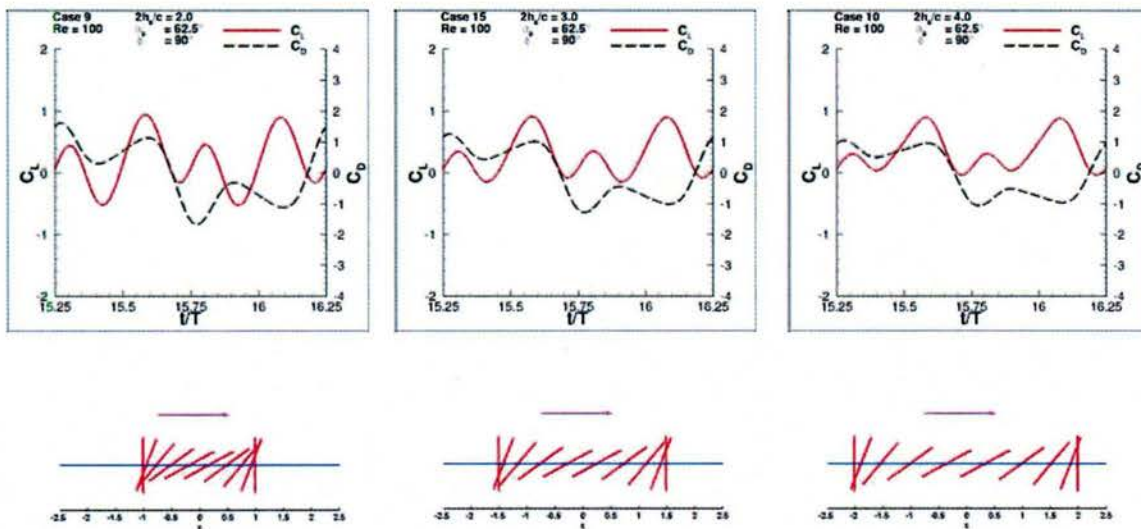

Figure 2.5-7. Snapshots of the effect of the plunging amplitude (2.0, 3.0, 4.0) on the instantaneous force history.

Angular Amplitude

In direct contrast to the discussion concerning the plunging amplitude, the design space is quite sensitive to the angular amplitude, see Figure 2.5-8. In general it is found that lower angular amplitudes, thus higher angles of attack, lead to higher power requirements and lift. The power required result is expected as higher angles of attack will correspond to more drag, and consequently a larger power requirement. The lift result, while not unexpected, is the result of interactions of the unsteady aerodynamics and is not entirely intuitive. What is evident is the fact that higher lift and lower power required aspirations are in direct competition on either end of the angular amplitude spectrum.
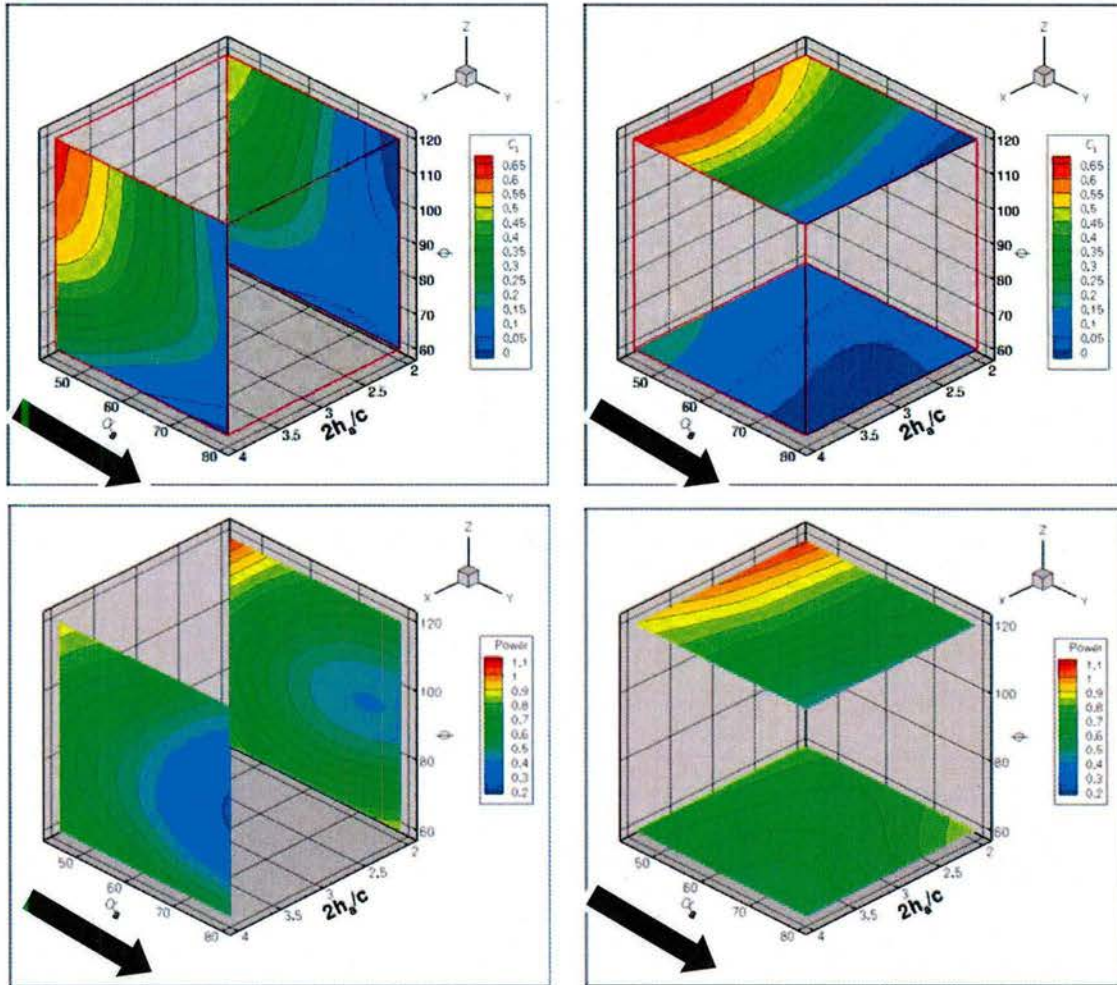
Figure 2.5-8. The lift coefficient (top) and power required (bottom) as approximated by the WAS illustrating the effect of the angular amplitude. A great deal of variance occurs with these changes and it is seen that in general lift coefficient over the whole cycle benefits from lower angular amplitudes. Arrows show the direction of increasing angular amplitude.

Looking again at force histories, the focus this time is angular amplitude, see Figure 2.5-9. The first observation is that the amplitude of the wake capturing peak does not change much with angular amplitude. This is somewhat surprising considering that higher angular amplitudes lead to higher angular velocities which then interact with the wake behind the airfoil at the end of the translation. The root of why the angular amplitude matters so much is seen clearly in the wake valley and subsequent delayed stall peak. As the angular amplitude is increased, and the angles of attack decreased, the airfoil approaches the jet at less favorable orientations, making the wake valley deeper and wider. However, the delayed stall peak also decreases and so we have two effects acting in concert. The lower angles of attack experienced do not provide diminished (and sometimes no) support for LEV formation and thus a much lower maximum lift value. At the same time, the higher angular amplitudes also provide a more streamlined body, producing less drag. It is seen that the rule of thumb is higher angles of attack and lower angular amplitudes provide higher lift through a combination of jet interaction and LEV, but at the same time create a higher drag.
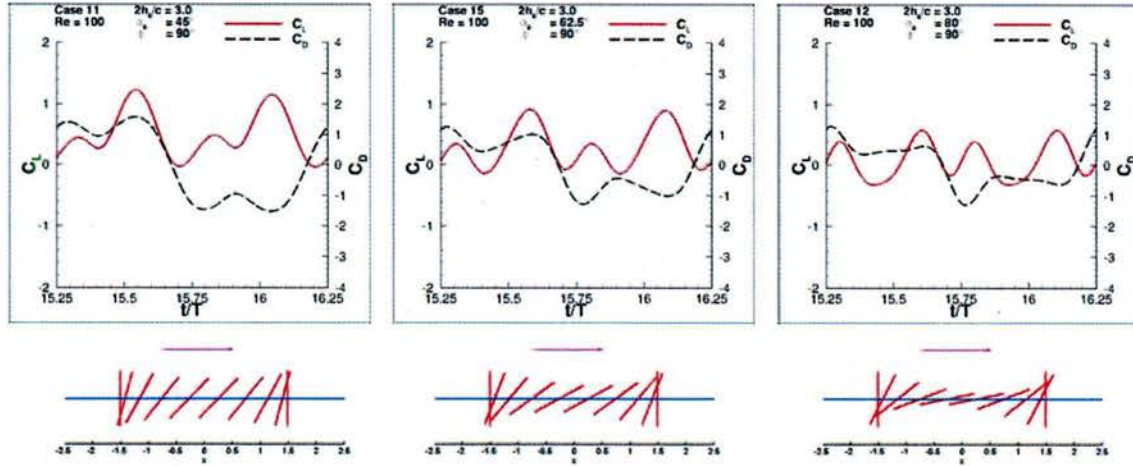
32

Figure 2.5-9. Snapshots of the effect of angular amplitude (45, 62.5, 80) on the instantaneous force histories.

Phase Lag

For the final design variable, phase lag, the general trend is for $\Phi > 90$, or advanced rotation, to produce higher lift values (Figure 2.5-10). How this occurs will be explained shortly but is once again a combination of unsteady effects. It is also interesting to note that the phase lag's influence on the integrated lift is minimal when angular amplitudes are high. Yet, at higher angular amplitudes is exactly where largest influence is felt when considering the power required. The fact that the most efficient mode, from an energy input perspective, is when $\Phi \approx 90$. This puts the minimum angle of attack at the maximum translational velocity, and therefore less drag and power required.

Coupled with the force histories in Figure 2.5-11, a more complete picture emerges. During $\Phi < 90$, or delayed rotation, the lift starts off negative and the wake capturing peak is shifted. From the illustrations of the airfoil positions, it can be seen that the airfoil is temporarily flying upside down and hence the negative lift occurs immediately upon changing direction. When the wake capture peak does occur it is also being influenced by the jet, and at the higher angles of attack the interaction is beneficial. The delayed stall peak suffers. Though there is a higher angle of attack occurring at the maximum translational velocity, as compared to $\Phi = 90$, the angular velocity is negative and not conducive to LEV formation.

33
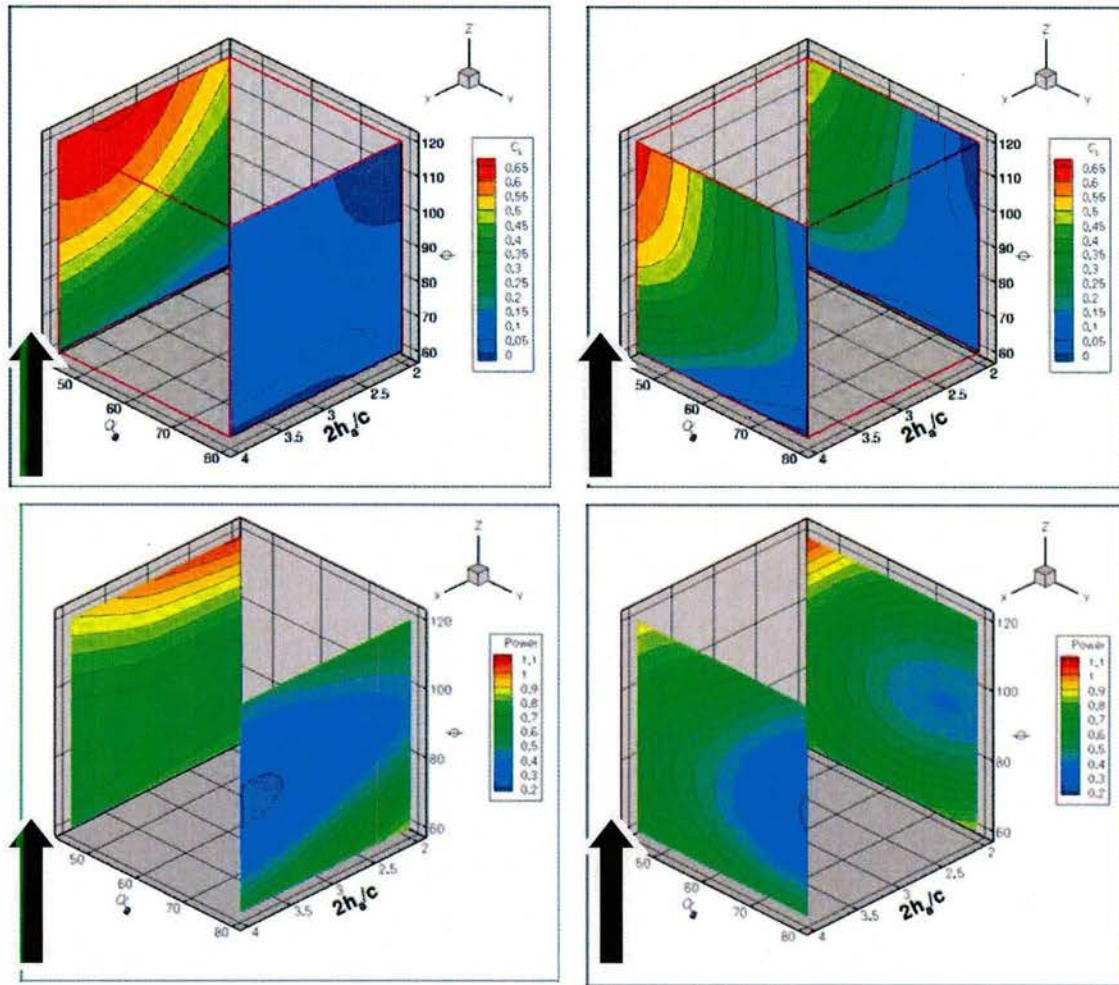
Figure 2.5-10. The lift coefficient (top) and power required (bottom) as approximated by the WAS illustrating the effect of the phase lag. Again a pronounced response in most areas of the design space. In general higher phase lags, corresponding to advanced rotation, are more beneficial from a lift point of view though that statement is not universally true, especially at higher angular amplitudes. Arrows show direction of increasing phase lag.

For $\Phi > 90$, or advanced rotation, the airfoil starts turning earlier such that a positive angle of attack is achieved upon wake capture, producing favorable lift. This is immediately followed by a pronounced wake valley. It was seen that when $\Phi = 90$, the wake valley could severely impede lift. That effect is exaggerated here where lower angles of attack encounter the jet. After that interaction, a very favorable delayed stall peak occurs as a higher angle of attack, with positive angular velocity, is present at the maximum translational velocity. While one can see from the surrogates the consequences of changing the phase lag, the variable's influence is more than initially implied. As seen from the force histories, the influences on the wake capture, jet interaction, and delayed stall partially cancel out thus obscuring its overall importance.

34
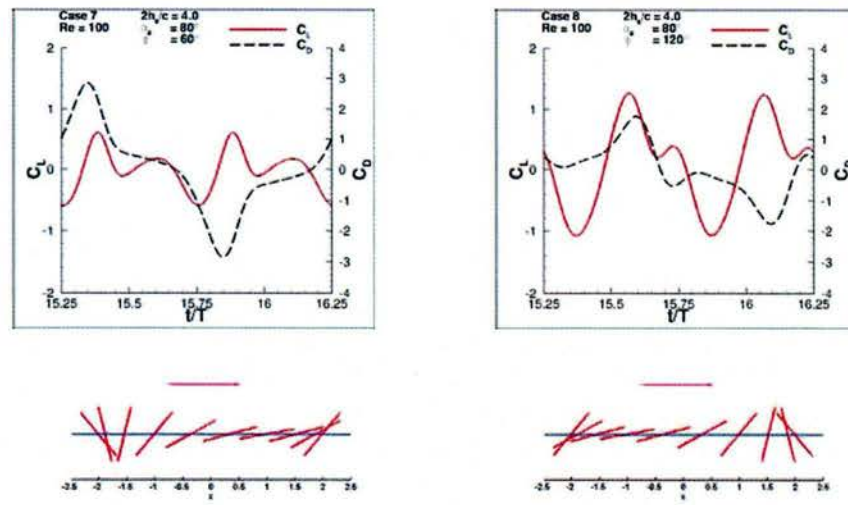
Figure 2.5-11. Force histories and airfoil positions illustrating delayed (left) and advanced (right) rotation. Here we see the utility in the advanced rotation as it keeps the lift levels high after the influence of the delayed stall has subsided.

2.5.6.4 Sensitivity Analysis
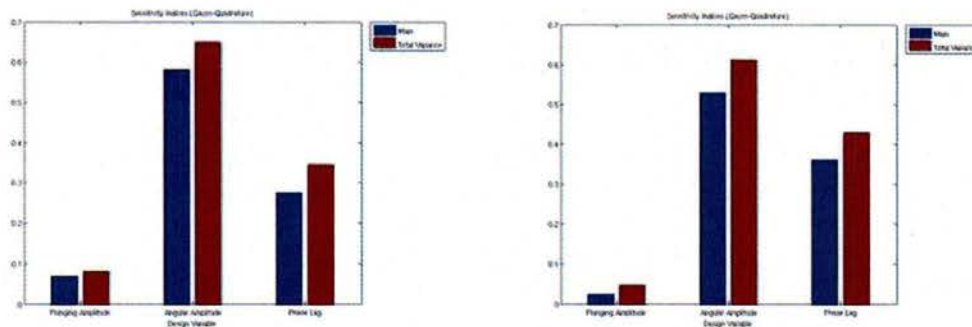
Figure 2.5-12. Sensitivity indices for $<C_L>$ (left) and $<P_{req}>$ (right) in normal hovering (no freestream). The main and total variances are given from left to right: plunging amplitude, angular amplitude, phase lag.

There is some sense of importance conveyed by the plots of the design space in Figure 2.5-6, Figure 2.5-8 and Figure 2.5-10. In low dimensions it may not be difficult to discern relative importance amongst the design variables. However, Figure 2.5-12 provides a more objective measure of influence. The global sensitivity indices are tabulated and a more quantifiable relationship can be determined. As expressed earlier, depending on whether instantaneous effects are important or whether the integrated result is sufficient, the role of phase lag could be underestimated. Regardless, within the design space examined, the plunging amplitude (and therefore the reduced frequency) plays a small role in determining the unsteady flow physics seen by an airfoil in normal hovering.

35
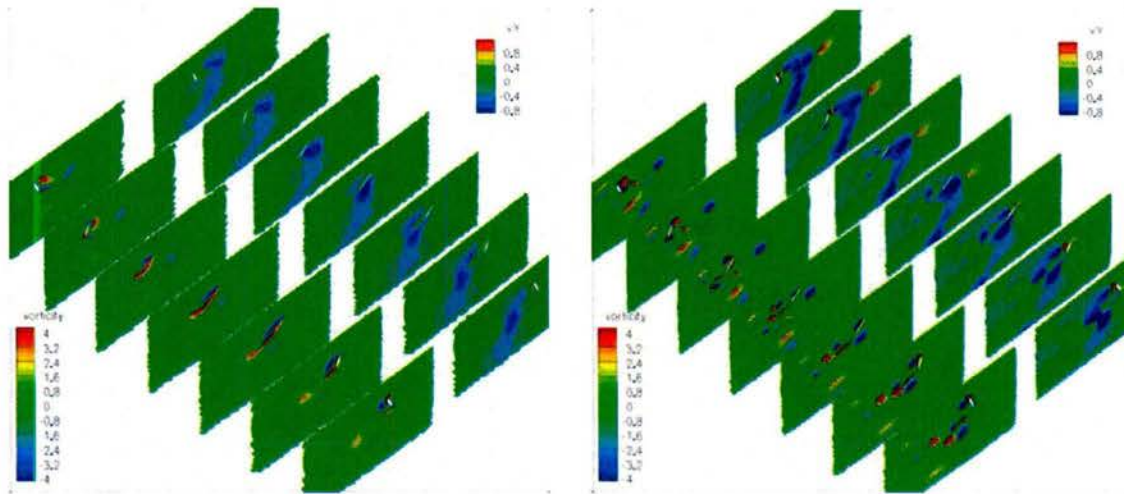
Figure 2.5-13. Vorticity and vertical velocity contour plots of normal hovering at Re=100 (left) and Re=1000 (right)

2.5.6.5 Reynolds Number

As the Reynolds number is increased, the vortex dynamics quickly lead to chaotic behavior. As seen in Figure 2.5-13, stronger vortices are created as the Reynolds number increases. These vortices persist and interact with each other over multiple stroke cycles which in turn leads to the chaotic force histories experienced by the airfoil (see Figure 2.5-14). Another implication of raising the Reynolds number is the strengthening of the jet-like flow feature which loses a stable configuration.
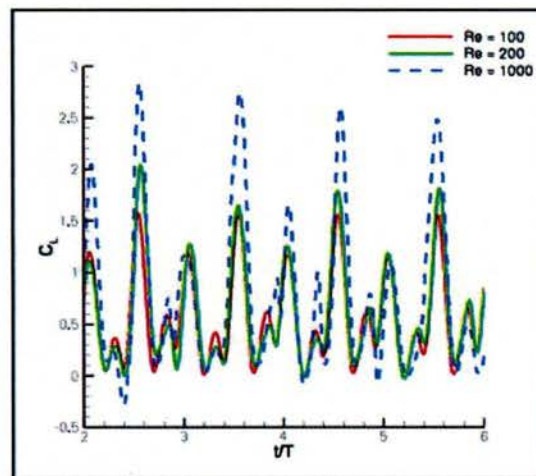
Figure 2.5-14. Reynolds number effect on C_L going from Re=100 (Red) which is displays a repeatable pattern, to Re=1000 (Dashed-Blue) whose force histories vary substantially from stroke to stroke.

To summarize, the work described in this section has addressed the following:

(1) Gain a better understanding of the 2D flow physics present in normal hovering:

The influence of kinematics, and the Reynolds number was investigated. Regarding the kinematics, it was found that under most of the circumstances studied, the plunging amplitude/ reduced frequency played a relatively minute role in determining the flow physics and consequent forces experienced by the airfoil. As the reduced frequency is one of the non-dimensional groups it was somewhat expected that the parameter would have a larger influence. A point of caution is warranted as the conclusions presented are taken in the context of the current design space. The flow quickly tended towards chaos due to the increased intensity and number of vortex interactions as the Reynolds number was increased.

(2) Demonstrate the utility of surrogate modeling in building a quantitative framework to assess hovering kinematics and the associated flow physics:

The WAS provided insight regarding general trends not easily extracted otherwise (e.g. examining the force histories at the DOE points). The global sensitivity evaluations quickly show the relative influence each design variable carries, and one can quickly evaluate a variable's importance. In the cases investigated above, the angular amplitude was always sensitive to small changes. As was explained, the influence of the phase lag was partially hidden by the competition in effects in the zero freestream cases, so one must exercise caution when making more general implications (e.g. In the present context of integrated values over the course of a cycle, the surrogates give what was asked of them. If one wanted to make conclusions about the instantaneous effects, one would have to look more closely at the flow physics, as was done, or redefine a proper objective function). It is also worth noting that most of the results show the design variables are largely uncoupled. An implication of this is that a simple liner superposition of design variable effects may suffice in the present context. In the work conducted so far, it is found that the WAS provides an efficient method for characterizing the flow physics and quantifying kinematic effects in normal hovering.

2.6 Coupling of Loci-STREAM and NLAMS for Fluid-Structure Interaction

During the last phase of the project, work was undertaken to couple the fluid-dynamics solver Loci-STREAM developed at Streamline Numerics Inc. (SNI) with the structural solver NLAMS (Nonlinear Membrane Shell Solver) developed at the University of Michigan (UM). As a first step, the requirements necessary to integrate the two codes were formalized. The following are some of the key outcomes of the collaboration:

1) Due to the relatively small computational requirements of the structural solver compared to the fluids solver, it was decided that no attempt would be made to parallelize the existing structural solver. Thus, the existing implementation of structural solver will compute the entire structural dynamics problem for the wing on each process, while the fluid dynamics solver will partition its part of the combined application over multiple processes, each solving only its portion of the domain. The only limitation of this approach is the requirement that the complete structural dynamics problem (for the whole wing for example) be capable of residing in memory on each process without causing paging from the system disk to system RAM. Due to the small size of the structural dynamics meshes currently being used for the flapping-wing problems (less than 10,000 cells), this requirement is easily met. When larger meshes are used for the structural dynamics part of the calculation (estimated to be greater than several hundred thousand cells), work will have to be undertaken to parallelize the structural dynamics solver. In addition, given the relatively small nature of the structural dynamics mesh (approximately 100 times smaller than the fluid dynamics mesh), no detrimental effect on the overall scalability of Loci-STREAM for the combined problem is anticipated.

2) An interface has previously been established between the structured solver STREAM and NLAMS. Since both of these solvers are written in Fortran 90, this interface relied heavily on the use of Fortran modules to communicate data bewtween the fluids and structural solvers. Since Loci-STREAM is written in C++ and thus cannot access variables via modules from Fortran 90, an interface wrapper was written for NLAMS which allows all global information required by NLAMS to be passed via function arguments.

3) The existing NLAMS interface was restructured and substantially simplified for use with Loci-STREAM. Due to the nature of Loci-STREAM it was deemed difficult to implement the fluid/structure iteration loop which was used to coordinate the combined fluid and structures calculations between the structured solver STREAM and NLAMS. Thus, it was decided to dispense with the fluid/structure loop and instead use the existing iteration loop within Loci-STREAM along with a modulo input flag (NLAMS called once for every 10 fluid iterations, for example) to control the coupling between the fluid dynamics and structural dynamics problems.

With a clearly defined interface now established between NLAMS and Loci-STREAM, a CSD (Computational Solid Dynamics) module is being developed for Loci-STREAM which will gather all required data from the fluid dynamics mesh and solution required by NLAMS to solve the structural dynamics problem. In addition, a general restructuring of the existing Loci-STREAM grid motion module to support solution-dependent mesh deformation problems (problems in which the mesh deformation is a function of the flow solution as opposed to simply a time-dependent forced boundary) has recently been completed.

2.6.1   Test Case

As preparation for testing and validation of the fluid-structure capability using Loci-STREAM, computational models were set up to simulate an aluminium monolithic Zimmerman wing flapping at 10 Hz with +/- 17 or 21 degree amplitude by coupling the UM/NLAMS, MSC.Marc, and STREAM codes. A new grid topology was developed for this wing which helped overcome some of the re-meshing problems of STREAM. Two different views of the CFD mesh developed in Pointwise are given in Figure 2.6-1. It may be observed that one of the block interfaces previously at the "tip" is now moved more inboard. This had a major impact on the negative Jacobian problem which generally occurred in the tip region.

Computational meshes for fluid and structural simulation are built as shown in Figure 2.6-1 and Figure 2.6-2, respectively. Details of mesh resolutions are shown in Table 2.6-1 and Table 2.6-2. Note that in order to avoid problems in the re-meshing phase during the fluid computation, a slightly large first grid space is utilized for the "base" grid of the CFD model. For the CFD model, the distance of the outer boundary from the wing is $25c$ (0.625 mm) and the thickness of wing is zero. For the CSD model, the model called 'base' does not include a square rigid region near the wing root, whereas the models named 'medium' and 'fine' include this region. The thickness of the structure is 0.4 mm, and Young's modulus and density of the material (aluminium) are 70.0 GPa and 2700 kg/m^3, respectively. Two wing kinematics are considered: (a) $1 - \cos(\omega t)$; (b) $\sin(\omega t)$, where ω is the angular velocity of flapping motion. Flapping frequencies are 10 and 15 Hz. Flapping amplitudes are 17 and 21 deg. All parameters and dimensionless parameters are summarized in Table 2.6-3.
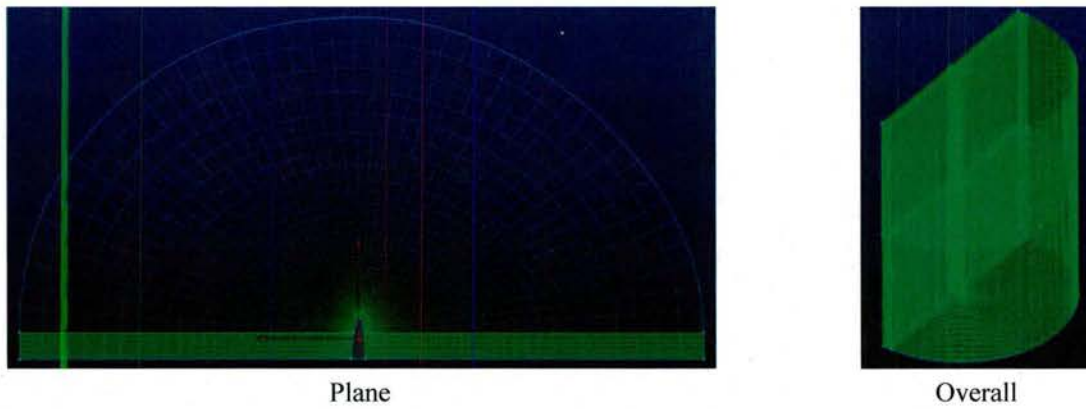
Plane   Overall

Figure 2.6-1. Images of computational mesh for fluid dynamics.

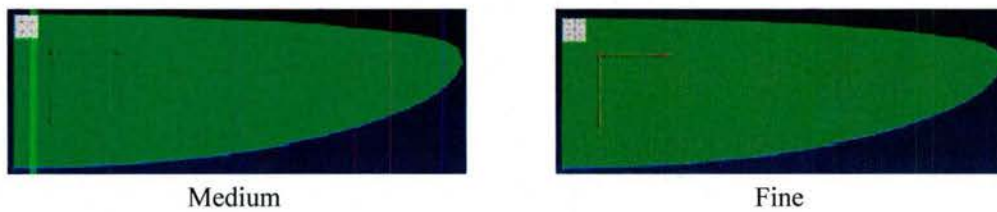Medium   Fine

Figure 2.6-2. Images of structural meshes.

Table 2.6-1. Computational meshes for fluid dynamics.

	Total number of cells	First grid spacing
Base	0.7 Million	2.5e-3 (0.1 c)
Medium	0.7 Million	1.0e-3 (0.04 c)
Fine	1.2 Million	5.0e-4 (0.02 c)

* c indicates length of wing root (0.025 mm)

Table 2.6-2. Computational meshes for structural dynamics

	Total number of elements	Root
Base	244	cantilevered
Medium	480	considered fixed root
Fine	774	considered fixed root

39

Table 2.6-3. Geometric, kinematics, and material parameters of UF's Zimmerman wing

Name	Nomenclature	Number & Unit
Wing length	b	75 mm
Chord length of wing root	C_{root}	25 mm
Aspect ratio	$AR=b^2/S$	7.65
Flapping frequency (input)	f	10-15 Hz
Flapping amplitude (input)	φ	±17° (34°) or ±21° (42°)
		±0.6108 rad (1.2216 rad)
Young's modulus of material	E_{alum}	70.0 GPa
Density of material	ρ_{alum}	2700 kg/m^3
Reference velocity	U_{ref}	0.89-1.65 m/s
Reynolds number	Re	1483-2750
Reduced frequency	k	0.714-0.882
Density ratio	ρ_{alum}/ρ_{air}	2.7
Elastic parameter	Π_1	9.66-33.1

Wing kinematics	Formula
Case 1	$1 - \cos(\omega t)$
Case 2	$\sin(\omega t)$

Experimental data for this case have been received from the University of Florida for the 10 Hz case using $sin\ (\omega t)$ as the wing kinematics. Grid sensitivity analysis was conducted and the results are shown in Figure 2.6-3. Based on these results, the medium grid will be employed for subsequent computations.
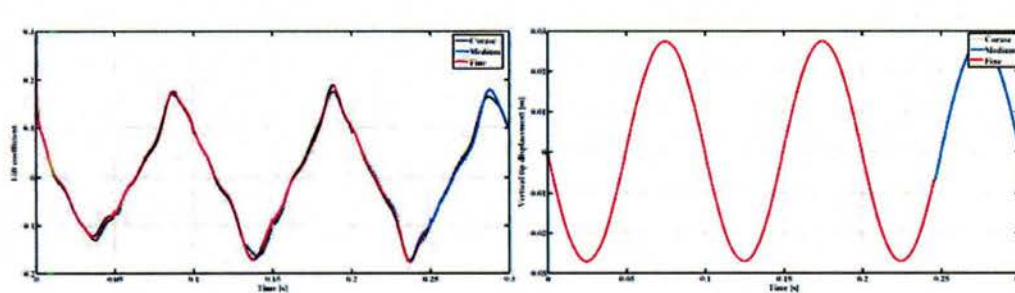
Figure 2.6-3. Time histories of lift coefficients (left) and vertical tip displacement (right) for three grid system

3. COMPUTATIONAL INVESTIGATIONS OF FLAPPING WING AERODYNAMICS

In this section, we report the results of the investigation of Reynolds number effects and shape effects on the flow field using two nominally two-dimensional airfoils (SD7003 and a flat plate) undergoing combined pitch- and plunge and pure plunge at Reynolds numbers 1×10^4, 3×10^4, and 6×10^4. The two different sets of kinematics represent a weak dynamic stall and a stronger dynamic stall, respectively. Experimental and computational flowfield results are compared: phase-averaged Particle Image Velocimetry (PIV) measurements are reported, and two-dimensional RANS equations coupled with Menter's Shear Stress Transport (SST). In addition, lift coefficient computed using unsteady linear airfoil theory (Theodorsen 1935) is compared with the computed lift coefficient. The focus of the investigation is to qualitatively and quantitatively ascertain the role of two-dimensional effects such as leading edge vortex formation, vortex shedding, and phase lag between flow field and the instantaneous angle of attack, tracing the flowfield and lift coefficient time histories. Issues such as flow variations in the spanwise direction, leading-trailing edge vortex interaction with the wing as well as tip vortices are not addressed here. But as a secondary objective, favorable comparison between experiment and computation would suggest that three-dimensional effects would not be of primary importance in either, for the range of motions presently under consideration.

3.1 Theodorsen's Unsteady Linear Airfoil Theory

One important issue in periodic oscillatory airfoil flows is the lag between the aerodynamic response and the airfoil motion kinematics. Quasi-steady models for lift coefficient have enjoyed some success even in high-frequency and geometrically-complex kinematics, such as the mechanical models of fruit-fly wings (Sane and Dickinson 2002). As a natural extension, constructing an explicit relation of the lag of putatively sinusoidal force response to sinusoidal motion kinematics, as a function of reduced frequency, amplitudes of pitch and plunge, phase difference between pitch and plunge, and the Reynolds number is necessary. This could then form a model for the lift response to more general motions and in more general configurations. Perhaps the simplest generalization beyond the quasi-steady approximation was obtained by Theodorsen (1935) model, for sinusoidal pitch-plunge of a thin airfoil, by assuming a planar wake and a trailing-edge Kutta condition, in incompressible inviscid flow. The lift coefficient time history is given by Eq. (3.1).

$$C_L(t) = 2\pi\left(1 - C(k)\right)\alpha_0 + \frac{\pi c}{2}\left\{\frac{\dot{\alpha}}{U_\infty} + \frac{\ddot{h}}{U_\infty^2} - \frac{c(2x_p - 1)\ddot{\alpha}}{2U_\infty^2}\right\} + 2\pi C(k)\left\{\frac{\dot{h}}{U_\infty} + \alpha + c(1.5 - 2x_p)\frac{\dot{\alpha}}{2U_\infty}\right\}.$$

(3.1)

The pitch and plunge motions are described by the complex exponentials, $\alpha(t) = \alpha_0 + A e^{i\{2\pi(ft+\phi)\}}$ and $h(t) = h_0 e^{2\pi f t i}$. The phase lead of pitch compared to plunge in terms of fractions of motion period is denoted by ϕ. In the most common case, motivated by considerations of maximum propulsive efficiency (Anderson et al. 1998), pitch leads plunge by 90°, which results in $\phi = 0.25$. The reduced frequency, k, is defined as $k = \pi f c / U_\infty = \pi St/(2h_0)$, and $C(k)$ is the complex-valued "Theodorsen function" with magnitude ≤ 1. It accounts for attenuation of lift amplitude and time-lag in lift response, from its real and imaginary parts, respectively. The first term is the steady-state lift and the second term is the "apparent mass" or noncirculatory lift due to acceleration effects. The third term models circulatory effects. Setting $C(k) = 1$ ($k = 0$) recovers the quasi-steady thin airfoil solution. The noncirculatory term follows instantaneously the kinematics of motion, but evolution of the wake yields phase lag relative to the kinematics of airfoil motion in the circulatory term, which is predicted to peak for k approximately equal to 0.3.
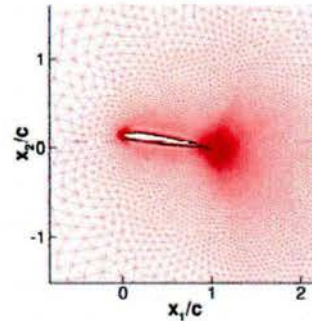
The simplicity of Theodorsen's model is a powerful advantage when running large parameter studies, but its accuracy for separated flows with obviously nonplanar wakes remains an issue of contention. In this study we compare the Theodorsen's solution to the RANS computation for lift coefficient to address the model's applicability at $Re = O(10^4)$ for the reduced frequency of $k = 0.25$.
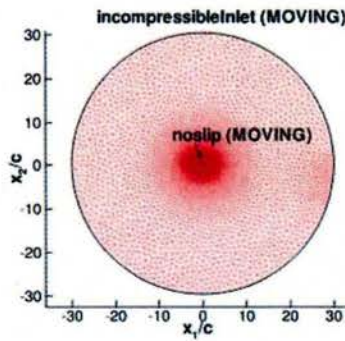
3.1.1   Computational domain and kinematics

The numerical solutions are computed in open bounded domain with Loci-STREAM on an unstructured grid with 46281, and 32204 mixed elements for the SD7003 airfoil, and flat plate, respectively, see Figure 3.1-1. The outer boundaries of the computational domain are 50 (Figure 3.1-1(a1)), and 30 chord lengths apart (Figure 3.1-1 (b1)), respectively. The thickness of the flat plate is 2.3% chord length and the leading and trailing edges are rounded (radius of 1.15 % chord length). The boundary conditions are as follows: on the airfoil no-slip conditions are imposed; the outer boundaries are incompressible inlets; and the inlet turbulence intensity is 0.5%. The computations are run assuming fully-turbulent, with no attempt to model transition or to prescribe the chordwise location of when to turn on the production term in the turbulence model.
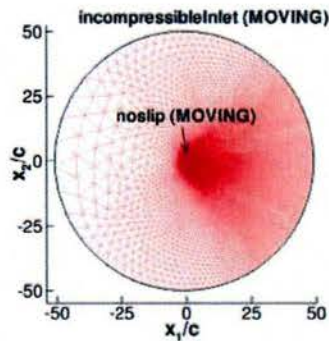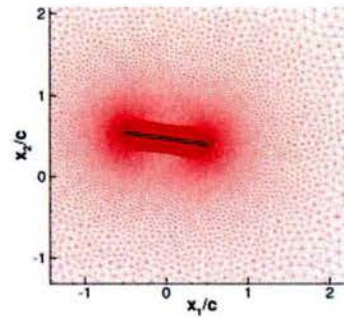

(a1) SD7003 airfoil in open bounded domain   (a2) Mixed elements near the SD7003 airfoil

(b1) Flat plate airfoil in open bounded domain   (b2) Mixed elements near the flat plate

Figure 3.1-1. Computational grid systems: (a) SD7003; (b) Flat plate.

The motion kinematics time histories are described by

$$h(t) = h_0 c \cos(2\pi t/T)$$
$$\alpha(t) = \alpha_0 + A\cos\{2\pi(t/T + \phi)\}$$

where h is the location of the center of rotation ($x_p/c = 0.25$) of the airfoil measured normal to the free stream, h_0 is the normalized amplitude of the plunge motion, T is the motion physical period, c is the airfoil chord, α is the geometrical angle of attack (AoA) measured relative to the incoming free stream with velocity, U_∞, α_0 is the mean angle of attack, and A is the amplitude of the pitching motion, see Figure 3.1-2.
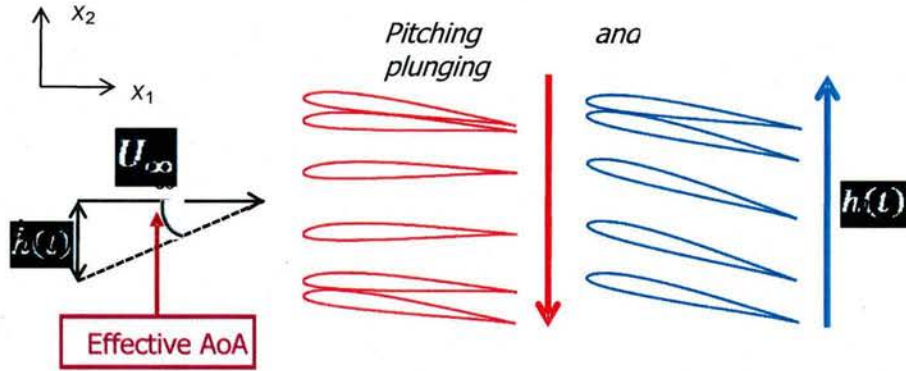

Figure 3.1-2. Schematic of SD7003 airfoil positions in downstroke (RED) and upstroke (BLUE), and the definition of the free stream direction and the effective angle of attack (effective AoA) due to plunging motion.

The effective angle of attack, α_e, is a linear combination of the pitching angle and the induced angle due to plunging motion, and can be written as,

$$\alpha_e = \alpha_0 + \lambda \arctan(\pi St) \cos\{2\pi(ft + \phi)\} + \arctan\{\pi St \sin(2\pi ft)\}$$

where $St = 2fch_0/U_\infty$ is the Strouhal number, and $\lambda = A/\arctan\{\max(\dot{h})/U_\infty\}$ is the ratio of the maximum effective angles of attack of the pitching motion to the plunge motion, where $\dot{h}$ is the plunge velocity, Figure 3.1-3. The Reynolds number is varied by changing the flow speed, $Re = U_\infty c/\nu$. It is clear from the kinematics that maintaining the same effective angle of attack time history requires a constant Strouhal number and constant λ. Thus, as Re varies, the reduced frequency, $k = \pi fc/U_\infty = \pi St/(2h_0)$, and the Strouhal number are kept constant by varying the physical frequency proportionately.

The choice of reduced frequency, $k = 0.25$, is motivated in part by cruise-type conditions for flapping flight of bird. Although the corresponding Strouhal number, $St = 0.08$, is below the range for maximum propulsion efficiency (Anderson et al. 1998), the present flow conditions are on the upper-end of the dynamic-stall literature, where the main application is helicopter blade aerodynamics (McCroskey 1982) , and for which the traditional analytical or phenomenological models in aeronautics tend to focus. As is often taken in applications motivated by maximizing propulsive efficiency of pitching and plunging motion, pitching leads plunging by one quarter of motion period: phase $\phi = 0.25$ and thus the airfoil "feathers", with the geometric pitching angle partially cancelling the plunge-induced angle of attack, $\arctan(\dot{h}/U_\infty)$. The pitching amplitude, A, is computed from the value of $\lambda = 0.6$ for the combined pitching and plunging case, while for the pure plunging case, $\lambda = 0$. The total effective angle of attack time-trace, α_e, straddles the static stall value of approximately $11°$ (Ol et al. 2005); this is just the sum of the pitching and plunging angles with appropriate phase shift.
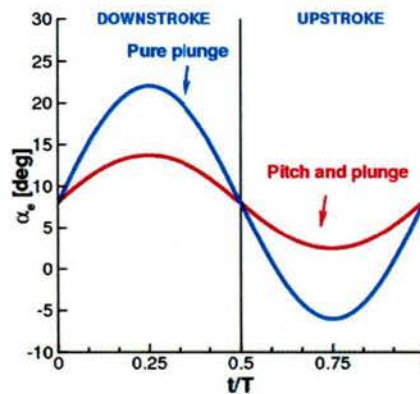
43

Figure 3.1-3. Time history of effective angle of attack (α_e) for the pitching and plunging kinematics (red line) and the pure plunging kinematics (blue line).

3.2   Spatial and Temporal Sensitivity Study

3.2.1   SD7003

Spatial and temporal sensitivity tests were performed for the pitch- and plunge case at Re=6×10^4, k = 0.25, and λ= 0.6. To assess the grid sensitivity time histories of lift coefficient on the baseline (46281 cells), finer
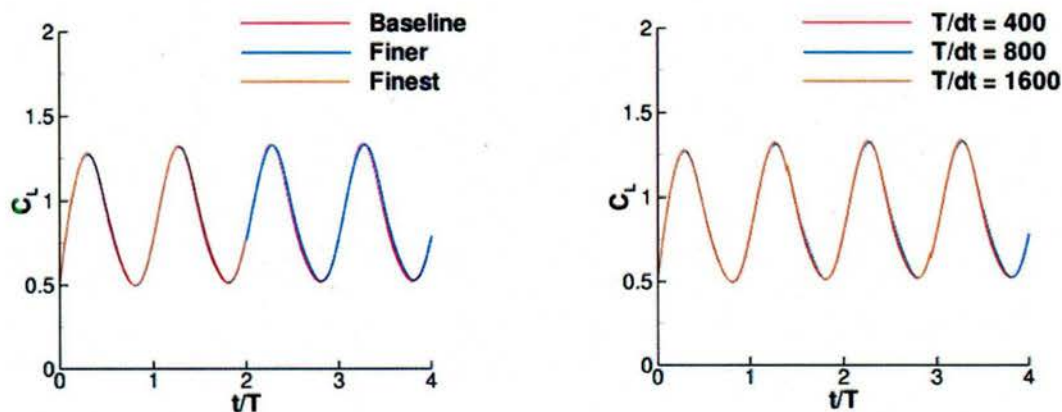
1 cells),
=6×10^4,
itching

(119951 cells) and the finest (368099 cells) grids are compared in Figure 3.2-1 (LEFT) using a time step of T/dt= 400. All three solutions coincide, and thus all subsequent computations are performed on the baseline grid. To investigate temporal sensitivity, three time steps were used: T/dt= 400, 800, and 1600. Figure 3.2-1 (RIGHT) shows that the computations using T/dt = 400 on the grid with 46281 cells is sufficient to obtain grid and time step-independent solution.

44

3.2.2   Flat Plate

For the pitching and plunging flat plate the spatial sensitivity test is investigated at Re = 6×10^4, k = 0.25, and λ = 0.6. To assess the grid sensitivity time histories of lift coefficient on the baseline (9624 cells), finer (32204 cells) and the finest (65904 cells) grids are compared in Figure 3.2-2 using a time step of T/dt = 480. All three solutions stay within maximum relative error of 2%, with the relative error between the finer and the finest grid smaller than between the baseline and the finer grid. Based on this observation, the finer grid has been chosen for all subsequent computations for the flat plate.
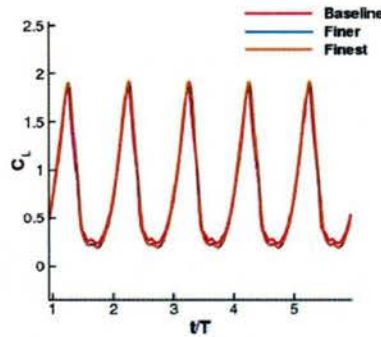

Figure 3.2-2. Time histories of the lift coefficients using the baseline (9624 cells), finer (32204 cells), and the finest (65904 cells) grid using T/dt = 480 over pitching and plunging two-dimensional flat plate at Re = 6×10^4, k = 0.25, and λ = 0.6.

3.3   Flow around a SD7003 Airfoil at Re= 6×10^4

3.3.1   Pitching and Plunging Case

Figure 3.3-1 shows the normalized mean streamwise velocity, u_1/U_∞, contours along with planar streamlines from the numerical and the experimental results from the UM and AFRL at t/T = 0.00, 0.25, 0.42, 0.50, and 0.75, respectively. The numerical solution with the modified SST turbulence model overpredicts the separation leading to generation of vortical structures at the bottom of the downstroke, t/T = 0.50, which is not observed in both PIV data. This is also illustrated in Figure 3.3-2, which shows u_1/U_∞-component velocity profiles at four different time instants at constant x_1/c= 0.25.

The overprediction of separation when using the modified SST model could be explained by the use of a limiter for the production term in the TKE equation. The build-up of turbulence near stagnation flow region is prevented, reducing the eddy viscosity in the RANS model. Figure 3.3-3 shows the local Reynolds number contours defined as $U_\infty c/(v+v_t)$ from the numerical computations using both SST turbulence closures at t/T= 0.25 for the pitching and plunging SD7003 airfoil. The limiter of the production in the TKE equation, see Eq. (1), enforced in the modified SST model results in substantially lower eddy viscosity, and hence higher local Reynolds number. Using the original SST turbulence model the viscosity ratio is at maximum near the leading edge. For the modified SST model, by limiting the production of TKE the local Reynolds number near the leading edge of the airfoil is close to 6×10^4, i.e. the amount of eddy viscosity in this region of the flow is small. Hence the flow tends to separate near the leading edge which is observed at t/T= 0.42 and 0.50 in Figure 3.3-1.

On the other hand, the agreement between the two experimental measurements is excellent, both in streamwise velocity contours as well as in streamlines. During the downstroke motion the numerical solution

with the modified SST model tends to predict larger reversed flow regions. The flow exhibits separation between the center of the downstroke and the bottom of the downstroke (Figure 3.3-1), corresponding to the maximum instantaneous effective angle of attack of 13.6°. Note that this value for the effective angle of attack is well beyond the static stall angle of 11°.
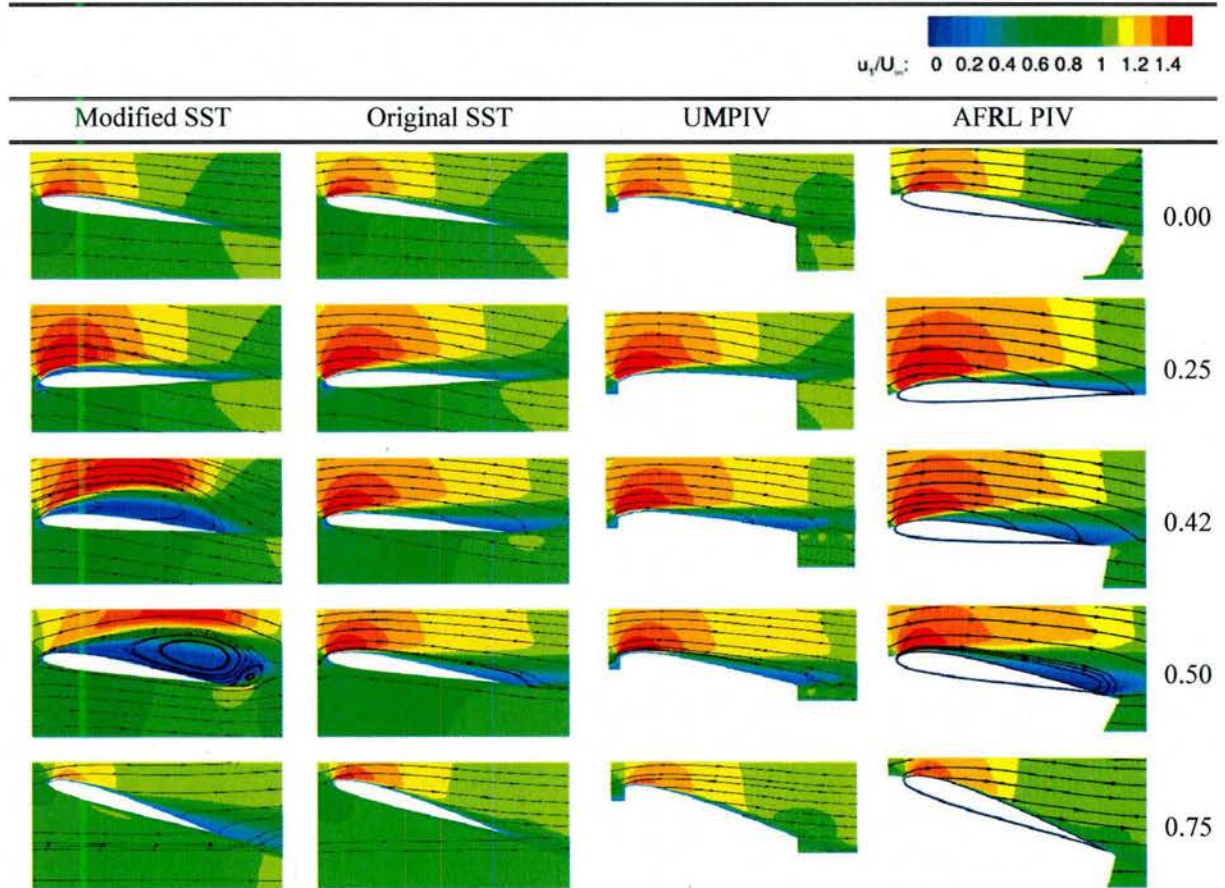

Figure 3.3-1. u_1/U_∞ **contours and the instantaneous streamlines over pitching and plunging SD7003 airfoil at k = 0.25, λ =0.6, and at Re = 6×10^4 from numerical (Modified SST, Original SST), and experimental (UM, AFRL) results.**
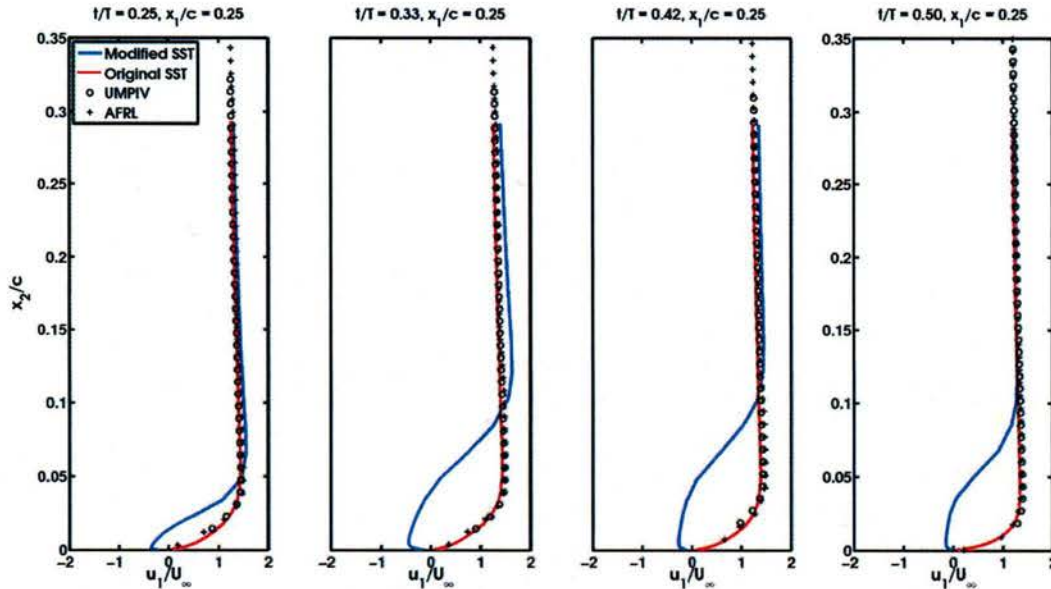
Figure 3.3-2. u_1/U_∞ profiles from numerical (Modified SST, Original SST), and experimental (UM, AFRL) results at t/T= 0.25, 0.33, 0.42, and 0.50 at constant x_1/c= 0.25 at Re = 6×10^4, k = 0.25, λ =0.6 for the pitching and plunging SD7003 airfoil.
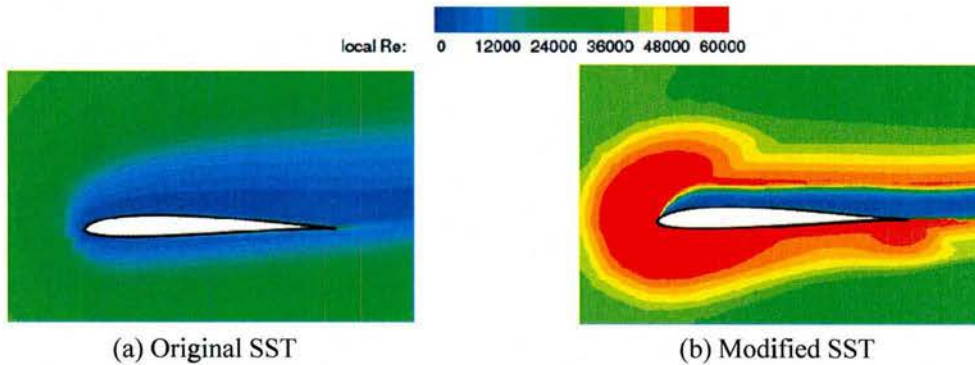

(a) Original SST   (b) Modified SST

Figure 3.3-3 Local Reynolds number contours using (a) the original SST, and (b) the modified SST at t/T= 0.25 for pitching and plunging SD7003 airfoil at Re= 6×10^4, k = 0.25, λ =0.6.

Lift coefficient time history is shown in Figure 3.3-4, comparing the quasi-steady ($2\pi\alpha_e$), Theodorsen, and computed values. Compared to the steady-state approximation, both Theodorsen's result and the computation show smaller lift amplitude as well as some phase lag indicating non-negligible influence from the wake via the circulatory terms in Eq. (1) at k = 0.25. Theodorsen's solution and numerical solution agree most closely at the phase 90°.At phase 180° the discrepancy is the largest, and hereboth numerical and experimental results show an open separation on the airfoil suction side (Figure 3.3-1). Since the Theodorsen's solution assumes a planar wake and Kutta condition at the trailing edge, the wake structure at phase 180° violates this condition causing the discrepancy in the lift coefficient. Overall, the Theodorsen's solution approximates the lift coefficient from the numerical computation better when the wake is 'planar'.
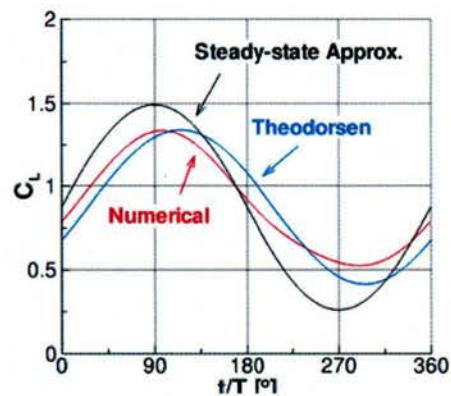
0.6).

3.3.2 Pure plunging case

Using the original version of SST turbulence model the computation showed a thinner but open separation, however the approach with the modified version of SST model the numerical result is able to predict the vortical structure with reattachment at $x_1/c \sim 0.8$ at $t/T = 0.25$.
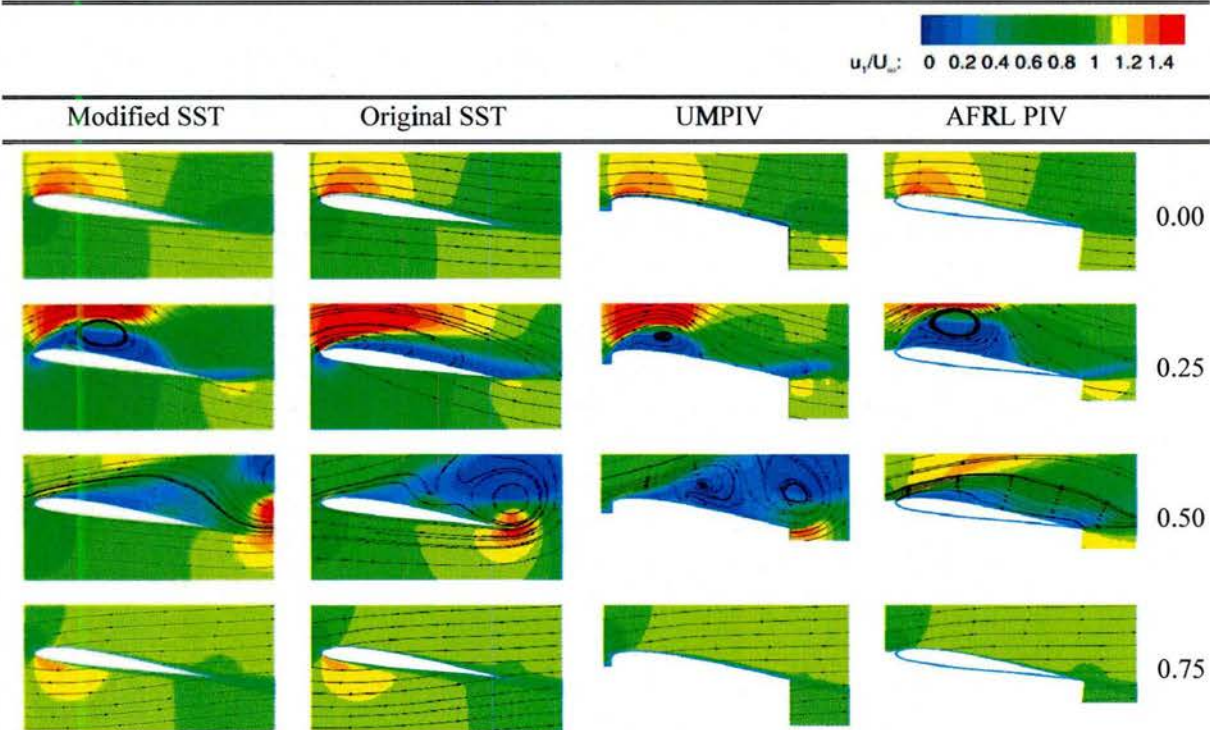

Figure 3.3-5. u_1/U_∞ **contours and instantaneous streamlines over pure plunging SD7003 airfoil at k= 0.25, λ =0.0, and at Re= 6×10^4 from numerical (Modified SST, Original SST), and experimental (UM, AFRL) results.**

48

Figure 3.3-5 shows the u_1/U_∞ contour plots and the instantaneous streamlines from the numerical computation and the experimental measurements from the UM and AFRL water tunnels for the pure plunging SD7003 airfoil at t/T = 0.00, 0.25, 0.50, and 0.75. The agreement between the computational and the experimental approaches is favorable when the flow is largely attached. When the flow exhibits massive separation, for example at t/T = 0.50, the experimental and computational results show noticeable differences in phase as well as the size of flow separation. The details of the vortical structures differ in all results; however, it is interesting to observe that the original SST model matched the PIV results from the UM facility better, while the modified SST model produced result more consistent with that from the AFRL facility. The consistent/inconsistent results appeared at t/T = 0.50 where a smaller vortical structure is evinced on the suction side of the airfoil in the UM facility, while in AFRL data such a vortical structure is hardly present.

As already discussed, the flow tends to separate more substantially under the modified SST model than under the original SST model due to different eddy viscosity levels predicted. The exact cause of the difference between the two PIV data is not clear right now. Based on the computational assessment, the effective inlet turbulence level of the two tunnels associated with the wing motion may be different.

Figure 3.3-6 compares the lift coefficient computed from quasi-steady ($2\pi\alpha_e$), Theodorsen and CFD for the pure plunging case. Theodorsen's solution and the numerical result coincide for t/T= 0.75 to t/T = 0.25 while between t/T = 0.25 and t/T = 0.50, the numerical solution shows higher frequency behavior and deviates from the analytic prediction both in amplitude and phase. Similar to pitching and plunging case, the wake structures in both PIV and CFD results are not planar (see Figure 3.3-3), violating one of the assumptions for the Theodorsen's solution. The phase lag between the effective angle of attack and the response of the aerodynamic loading is smaller than in the pitching and plunging case, despite the larger extent of flow separation.
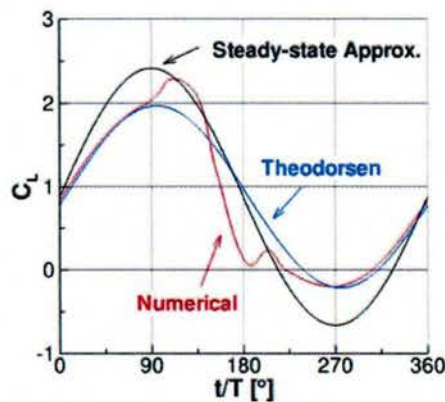

Figure 3.3-6. Time histories of lift coefficient for the pure plunge case (Re= 6×10^4, k = 0.25, λ=0.0).

Unlike the pitching and plunging case where the flow showed only thin open separation, the pure plunging case generates large vortical structures at the leading edge between motion phases of 90° and 120°. Subsequently, this structure – which may be called a leading edge vortex – broadens, weakens, and convects downstream, eventually enveloping the entire airfoil suction side. By 180° phase of motion, reattachment is evinced at the leading edge, and sweeps downstream as the airfoil proceeds on the upstroke. The LEV and its subsequent development enhance suction, and thus also lift. This is seen in Figure 3.3-6 as a broad peak in lift at phase between 90° and 120° in the numerical lift coefficient result, followed by a drop in lift. The

latter is associable with weakening and downstream convection of the LEV, and loss of leading-edge suction. Figure 3.3-7 shows the computed pressure coefficient contours, and normalized vorticity contours from both the numerical and the experimental results at the phase 90°.
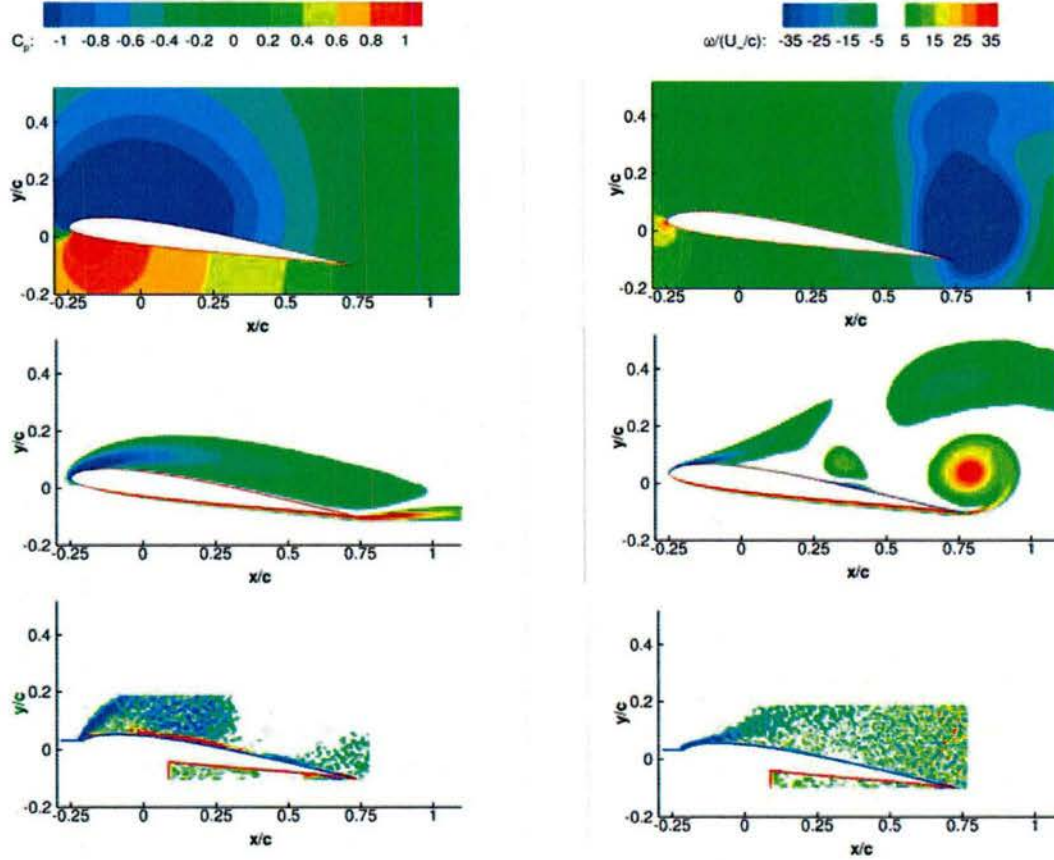

Figure 3.3-7. Pressure coefficient contours from the numerical computation (TOP), normalized vorticity contours from the numerical computation (MIDDLE), and normalized vorticity contours from the experimental measurements (BOTTOM) at the phases 90° (LEFT), and 180° (RIGHT) for the pure plunge case (Re = 6×10^4, k = 0.25, λ=0.0).

The LEV is notable in the experimental result, and to a lesser extent in the computation. At 180° the attenuation in vorticity peak values is consistent with the velocity contour plots and with the loss of suction near the leading edge, but there is a notable discrepancy between experiment and computation: the latter shows a strong trailing edge vortex, while the former does not. Most likely, this is the results of poor repeatability of the TEV from period to period, and thus its dissipation in the phase-averaged PIV results. Curiously, the experimental and the computational disagreements seem to be localized to the trailing edge, whence it may be inferred that discrepancy in overall lift would be small in the integrated sense. This, however, would require substantiation when direct measurement of lift becomes available in the experiment.